



Wall turbulence perturbed by a bump with organized small-scale roughness: coherent structure dynamics

Edgardo García¹ , Fazle Hussain¹ , Jie Yao^{1,2}  and Eric Stout^{1,3} 

¹Department of Mechanical Engineering, Texas Tech University, Lubbock, TX 79409, USA

²Advanced Research Institute of Multidisciplinary Sciences, Beijing Institute of Technology, Beijing 100081, PR China

³Naval Undersea Warfare Center, Newport, RI 02841, USA

Corresponding author: Edgardo García, edgardo.garcia@ttu.edu

(Received 1 July 2024; revised 7 November 2024; accepted 16 December 2024)

Coherent structures over two distinct, organized wall perturbations – a transverse sinusoidal bump with and without small-scale longitudinal grooves – are studied using direct numerical simulations. Large-scale spanwise rollers (SRs) form via shear layer rollup past the bump peak, enveloping a large separation bubble (SB) for both a smooth wall (SW) and a grooved wall (GW). In a GW, small-scale alternately spinning jets emanating from the crests' corners merge with the shear layer, altering the SRs compared with SRs in a SW. The underlying coherence of the highly turbulent SRs is deduced via phase-locked ensemble averaging. Coherent vorticity contours of SRs are ellipses tilted downward, hence causing co-gradient Reynolds stress. The limited streamwise length of SB precludes SR tumbling, unlike in a free shear layer. The coherent field reveals minibubbles attached to the bump's downstream wall with circulation opposite to that of the SB – they are larger, stronger and more numerous in GW than in SW – reducing skin friction. Compared with SW, the swirling jets in GW increase coherent production while decreasing incoherent production. Additionally, the jets push the SRs to travel faster and farther before reattachment. The SB experiences two different modes of oscillation due to high-frequency advection of the shear layer SR and low-frequency breathing of the SB, where the former dominates in GW and the latter in SW. Negative production is caused by counter-rotating vortex dipoles inducing flow ejections (for both SW and GW) and single vortices penetrating the grooves – both occurring in the region of flow acceleration.

Key words: boundary layer separation, vortex dynamics

1. Introduction

The dynamics of turbulent flows is known to be dominated by ‘coherent structures’ (CSs), which control features such as energy and momentum transports, particularly drag, heat and mass transfer and aeroacoustic noise generation (Hussain 1986; Jiménez 2018). For example, Zaman & Hussain (1981) showed that controlled excitation in free shear layers (plane mixing layer, and circular and plane jets) could suppress the formation of the naturally occurring energetic large-scale CSs, leading to reduced turbulence; not surprisingly, Hussain & Hasan (1985) subsequently showed a corresponding excitation-induced notable noise reduction in free jets. In turbulent boundary layers (TBLs), numerous studies have shown that skin friction can be notably decreased via active or passive control of near-wall CSs (Choi, Moin & Kim 1994; Gatti & Quadrio 2016; Yao, Chen & Hussain 2018; Duong, Corke & Thomas 2021). This clearly suggests promising benefits of CS control in various technological applications. In fact, control of a turbulent shear flow is possible only in the presence of CSs – no CS, no control (Hussain 1986).

1.1. Motivation

As CSs dominate many important flow statistics, it is reasonable to then expect certain dynamics, such as drag, as driven by specific CS features. For complex flows, such as the grooved wall with a spanwise bump (involving favourable and adverse pressure gradients as well as roughness) studied by Hussain *et al.* (2024), heavily modify CSs and hence the various features obtained in the mean flow. Hence, the underlying motivation of this paper is to use CSs to address those features and to explore other phenomena that may arise via CS studies.

1.2. Coherent structure eduction

While control of turbulent flows via the prevalent CS is now widely recognized, it is important to realize that CS occurs randomly in space and time, as well as in geometry, size, orientation, strength and states of evolution and mutual interaction (including pairing, tearing and reconnection). These present formidable challenges to objectively characterizing/quantifying CSs. The CSs are typically identified by flow visualizations, conditional sampling techniques (Wallace, Eckelmann & Brodkey 1972; Antonia 1981), proper orthogonal decomposition (Berkooz, Holmes & Lumley 1993) and more sophisticated eduction methodologies such as the phase-locked ensemble average (Reynolds & Hussain 1972). In the eduction process, selection of the threshold and bandwidth in the various metrics of CS is indeed subjective depending on the researchers insight and experience – intuitively optimized to yield results fairly insensitive to the values of the criteria. Here, we will focus on the eduction techniques based on the vorticity field. Hussain & Hayakawa (1987) used the vorticity for extracting the dominant large-scale CS using multiple linear rakes of X-hot-wire arrays in a turbulent wake behind a circular cylinder. Note that vorticity-based eduction methods are preferred due to the clearer structures observed, as velocity (following the BiotSavart law) extends much further from the structure’s centre, resulting in unclear boundaries. Jeong *et al.* (1997) later extended it to extract three-dimensional (3-D) CSs from direct numerical simulations (DNSs) of a turbulent channel flow. More recently, Hickey, Hussain & Wu (2013) performed a detailed analysis of CSs in the far wake, elucidating the CS organizations and their evolution using DNS.

1.3. *Coherent structure in turbulent boundary layers*

Coherent structure in flat plate TBLs has been the subject of numerous experimental and computational studies (Wark & Nagib 1991; Jeong *et al.* 1997; Nickels & Marusic 2001; Schoppa & Hussain 2002; Adrian & Marusic 2012; Schlatter *et al.* 2014; Jiménez 2018). The near-wall low-speed streaks (Kline *et al.* 1967) and the associated overlying quasi-streamwise vortices (Robinson 1991) are recognized to be integral to sustaining turbulence (Hamilton, Kim & Waleffe 1995; Panton 2001; Schoppa & Hussain 2002).

Because of their relevance to many flows in nature and technology, TBL studies have been pursued extensively to address the effects of pressure gradients, as well as roughness – both having significant effects on TBL behaviour. Of particular significance to many industrial and aerodynamic flows is the ubiquitous phenomenon of flow separation from a strong adverse pressure gradient, which itself has a vast literature. These two classes (TBLs with separation and roughness) of flows are relevant to this study and are reviewed briefly below.

1.4. *Coherent structure in separated flows*

A strong adverse pressure gradient (APG) in a TBL can lead to flow separation, often followed by reattachment, forming a separation bubble (SB) (Simpson 1991). As the flow approaches the separation point, it decelerates, and the streaks disappear. The dynamics surrounding the separation point, particularly that of the vortices, warrants careful studies. Interestingly, the near-wall region of the SB does not have streaks and wall-parallel vortices, presumably due to the low speed of upstream-moving flow. Past the separation point, the resulting planar shear layer rolls up into large-scale spanwise rollers (SRs) via Kelvin–Helmholtz instability (Simpson 1989; Schatzman & Thomas 2017). These rollers evolve as they advect downstream and even undergo pairing like those in a plane free shear layer. They dominate the generation of coherent Reynolds shear stress and turbulence production (Simpson 1991). Also, SRs are partially responsible for the movement of the reattachment location and the global unsteadiness of the turbulent SB (Kiya & Sasaki 1985). The structures of the far upstream TBL predominantly affect the detachment unsteadiness and upstream separation. Two distinct modes have been identified for the movement of detachment and reattachment: a high-frequency mode linked with the SRs (Na & Moin 1998) and a low-frequency ‘breathing’ motion (Wu, Meneveau & Mittal 2020).

1.5. *Coherent structure over rough walls*

The wall roughness naturally can also modify the near-wall flow dynamics (Jimenez 2004; Leonardi *et al.* 2004; Orlandi, Leonardi & Antonia 2006). For example, Talapatra & Katz (2012) showed that an array of identical pyramids induces horseshoe vortices contrasting with the typical quasi-streamwise vortices. Similarly, longitudinal grooves (akin to extensively studied riblets) can induce coherent secondary motions, altering the near-wall flow dynamics (Goldstein & Tuan 1998; Hwang & Lee 2018; Castro *et al.* 2021). Additionally, certain riblet shapes trigger a Kelvin–Helmholtz instability, exciting the formation of large-scale SRs across multiple riblets at the crests heights (Endrikat *et al.* 2021; García-Mayoral & Jiménez 2011).

Despite its importance in practical applications, the roughness effect on CSs in separated flows has received limited attention. Wu & Piomelli (2018) and Song & Eaton (2002) found that the roughness strongly influences turbulence intensities on top of the SB, as well as the SB size. However, these flow modifications have not yet been explained in terms of CSs.

1.6. *Negative production*

The (time-averaged) production of turbulent kinetic energy typically is positive, meaning a transfer of kinetic energy from the mean flow to turbulence to replenish energy lost to dissipation in the thermal form, but it can also be negative, although seldomly, representing an average transfer of energy from turbulence to the mean flow. Of course, the transfer of turbulent kinetic energy to the mean flow can only occur locally but obviously not globally. Even when occurring locally, such average counter-gradient transport is rare and needs careful examination. Instances of negative production have been reported in the literature. Here, we will mention only a few.

In turbulent channel flows with asymmetric boundary conditions or in turbulent wall jets where the zero Reynolds shear stress does not coincide with the zero mean velocity gradient, there can be regions of negative production (Hussain 1986). Some streamwise inhomogeneous flows also show negative production, such as in the shear layers of separating and reattaching flows (Cimarelli *et al.* 2019; Elyasi & Ghaemi 2019) and in ducts with varying cross-sectional area (Gence & Mathieu 1979) due to counter-gradient Reynolds shear stress and stretching of fluid. Similarly, this negative production due to stretching of fluid and counter-gradient Reynolds shear stress can happen in turbulent channel flows in regions of favourable pressure gradient (FPG) over bump perturbations (Banchetti, Luchini & Quadrio 2020; Selvatici, Quadrio & Chiarini 2023), discussed in detail in Hussain *et al.* (2024) (hereinafter referred to as HGYS). These examples identified local zones of negative production from statistical data without addressing the flow structure. However, Zaman & Hussain (1980) explained via CS dynamics that negative production regions can arise when vortex pairing with certain orientations favouring counter-gradient Reynolds shear stress occurs successively at the same location (shown by them under controlled excitation of a shear layer). In unexcited shear layers these negative production configurations of CS occur randomly in space and time so that the average production is positive everywhere. Negative production can happen even in the absence of pairing: for example, if an elliptical SR's orientation tilted downstream repeats successively at the same physical location. As we will see, in our case, a particular CS dynamics sequence repeats successively at the same location in space and time – thus yielding locally mean negative production, although different from that in Zaman & Hussain (1980).

1.7. *Paper layout*

In the following § 2, we first define the computational domain, describe the flow simulation database, define the averaging procedures utilized, summarize key flow statistics features from HGYS and delineate the objectives of the present paper. To further motivate the discussion, sample visualizations of instantaneous flow structures are provided in § 3. Mean flow field measures to identify global features of the CS are in § 4. The dynamically relevant CS are analysed in § 5 by a phase-average eduction technique. The effect of the grooved wall (GW) on the dominant CS and how these change the unsteadiness of the SB with respect to a smooth wall (SW) is discussed in § 6. Average negative productions occurring in two regions, involving two distinct mechanisms, are explained through the CS dynamics in § 7. Finally, § 8 summarizes the key findings.

2. **Methods and objectives**

2.1. *Flow simulation*

We study a turbulent channel flow with simple small-scale organized roughness elements (longitudinal grooves) in combination with a large-scale wall curvature perturbation

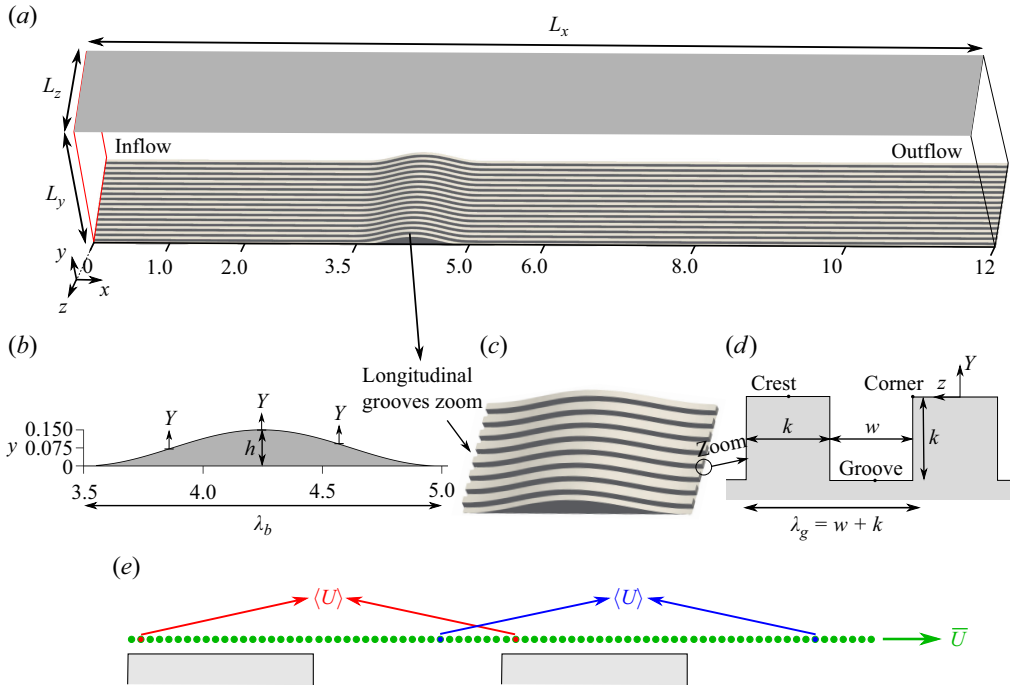


Figure 1. Computational domain and boundary conditions. (a) Simulation domain with inflow and outflow conditions (precomputation domain not shown; see HGYS); (b) bump profile parameter definitions; (c,d) groove geometry description and parameter definitions. The Y vertical coordinate starts at the crest at every x , and the y (global) coordinate starts at the bottom wall height away from the bump and is not a function of x . (e) Visual reference for the averaging procedures: \bar{U} is the average over all grid points in z (green dots) and $\langle U \rangle$ over either red dots only or blue dots only is shown as a reference. Hence \bar{U} is over 640 points while $\langle U \rangle$ is over 16 points. Note also $\langle U \rangle$ is a function of y and z and \bar{U} is a function of y only.

(a spanwise bump). The bump is large enough to generate flow separation yet sufficiently small that it does not notably alter the external flow, while the small-scale organized grooves have a notable effect on the dynamics of the separated flow. This flow configuration was considered by HGYS, and is used here to report further results on our earlier paper addressing the CSs responsible for the flow alterations caused by the bump and grooves. More details are given in HGYS; here, we summarize some key parameters.

The Cartesian coordinate system is denoted by (x, y, z) or (x_1, x_2, x_3) , where (x, x_1) is streamwise, (y, x_2) wall-normal and (z, x_3) spanwise; (U, V, W) or (U_i) are the corresponding instantaneous velocity components; and P is the pressure. All quantities are non-dimensionalized using the bulk velocity, U_b^* , half-height of the channel, H^* , and kinematic viscosity, ν^* ; dimensional quantities are starred. The friction Reynolds number at the channel's inlet is $Re_\tau = u_\tau^* H^* / \nu^* \approx 300$ ($u_\tau^* = \sqrt{\tau_w^* / \rho^*}$ is the friction velocity where τ_w is the mean wall shear stress and ρ the density; details of the computation of τ_w are given in HGYS). As shown in figure 1(a,b), the bump starts at $x = 3.5$ ($x^+ = 1050$) from the inlet, and its height is $h = 0.15$ ($h^+ = 45$). Here, the superscript $+$ denotes non-dimensionalization by u_τ and u_τ / ν at the inlet. For the GW case, square grooves with depth $k = 0.05$ ($k^+ = 15$) and pitch $\lambda_g = k + w = 0.1$ are considered (figure 1c,d). The number of grid points is $1280 \times 384 \times 640$ on a computational domain $(L_x, L_y, L_z) = (12, 2, 1.6)$; equally space grid cells are used in the x and z directions while stretching is employed in y . For this study, to have high resolution in time and maintain the database

size manageable, we limit ourselves to saving the data only for the region containing the bump and separated region (i.e. $3.5 \leq x \leq 9$, $y \leq 0.45$ and the whole span of the domain $0 \leq z \leq 1.6$). Analyses are performed using 6500 velocity fields, with an interval of 0.004 eddy turnover times (H/u_τ).

2.2. Averaging operators and the triple decomposition

The notation of averaging operators in HGYS is repeated, and an additional operator is defined here. In the case of SW, $\overline{(\cdot)}$ is used, which denotes time and spanwise averaging of all z points (covering the entire span; 20 points in each groove or crest, [figure 1e](#)). The fluctuation of any quantity with respect to the average $\overline{(\cdot)}$ is denoted by a lowercase letter; for example, the streamwise velocity fluctuation in SW is $u = U - \overline{U}$. For GW, in addition to $\overline{(\cdot)}$, the $\langle \cdot \rangle$ averaging procedure is used, which denotes time and spanwise average over all grooves at the same relative positions ([figure 1e](#)); the corresponding fluctuating quantity is denoted with a prime, i.e. $u' = U - \langle U \rangle$.

The fluctuating flow field in the Reynolds decomposition – either in $U = \overline{U} + u$ or $U = \langle U \rangle + u'$ – can be further decomposed into coherent and incoherent (random) parts. The CS flow field is obtained by first computing an ensemble average of phase-aligned realizations of structures with similar flow features (Jeong *et al.* 1997). Note that phase refers to the occurrence of an instantaneous flow structure at a particular stage of its evolution, and the phase is selected on the basis of each advecting CS vorticity pattern and peak value. Note also that vorticity distribution, contour shape and peak values vary from realization to realization. The ensemble average at a given phase of the structure is defined as

$$[U(x, y, z, t)] = \lim_{N \rightarrow \infty} \frac{1}{N} \sum_{m=1}^N U(x, y, z, t + t_m), \quad (2.1)$$

where t_m denotes the random time of occurrence of successive structures of the selected phase at a (x, y, z) location, called a station (Hussain & Reynolds 1970). If the structures pass the station at regular intervals, this definition reduces to a periodic phase average. The triple decomposition (in GW) of the velocity is $U = \langle U \rangle + \tilde{u} + u''$, where the coherent part is $\tilde{u} = [U] - \langle U \rangle$ (i.e. the CS flow field) and u'' is the incoherent (random) part. For simplicity and clarity in the following discussions, the quantities \tilde{u} and u'' are obtained using \overline{U} in SW and $\langle U \rangle$ in GW, and no new names are defined.

2.3. Summary of the earlier part of this work (HGYS)

The flow statistics of a turbulent channel flow with a spanwise bump and longitudinal grooves are extensively discussed in HGYS, and a summary of the important results are shown in [figure 2](#). On the upstream side of the SW bump, incipient (not observed in the mean statistics but noted in instantaneous visualizations) flow separation due to mean streamline curvature was observed. The grooves transform the incipient separation into a mean (steady in time) SB within the grooves. This effect of augmenting incipient into a steady separation in regions of pressure gradients due to mean streamline curvature is what generates the mean secondary SB (minibubble) inside the upstream-moving fluid at the bottom of the GW SB. Similar to the SW's incipient SB upstream of the bump, an opposite circulation minibubble is also present in SW, but occurs only sporadically. Through CS eduction, we show that these minibubbles are connected to the overall SR dynamics, detailed in § 5. The peak of turbulence intensity occurring in the shear layer past the bump peak (region VII in [figure 2a](#)) decreases due to the presence of grooves.

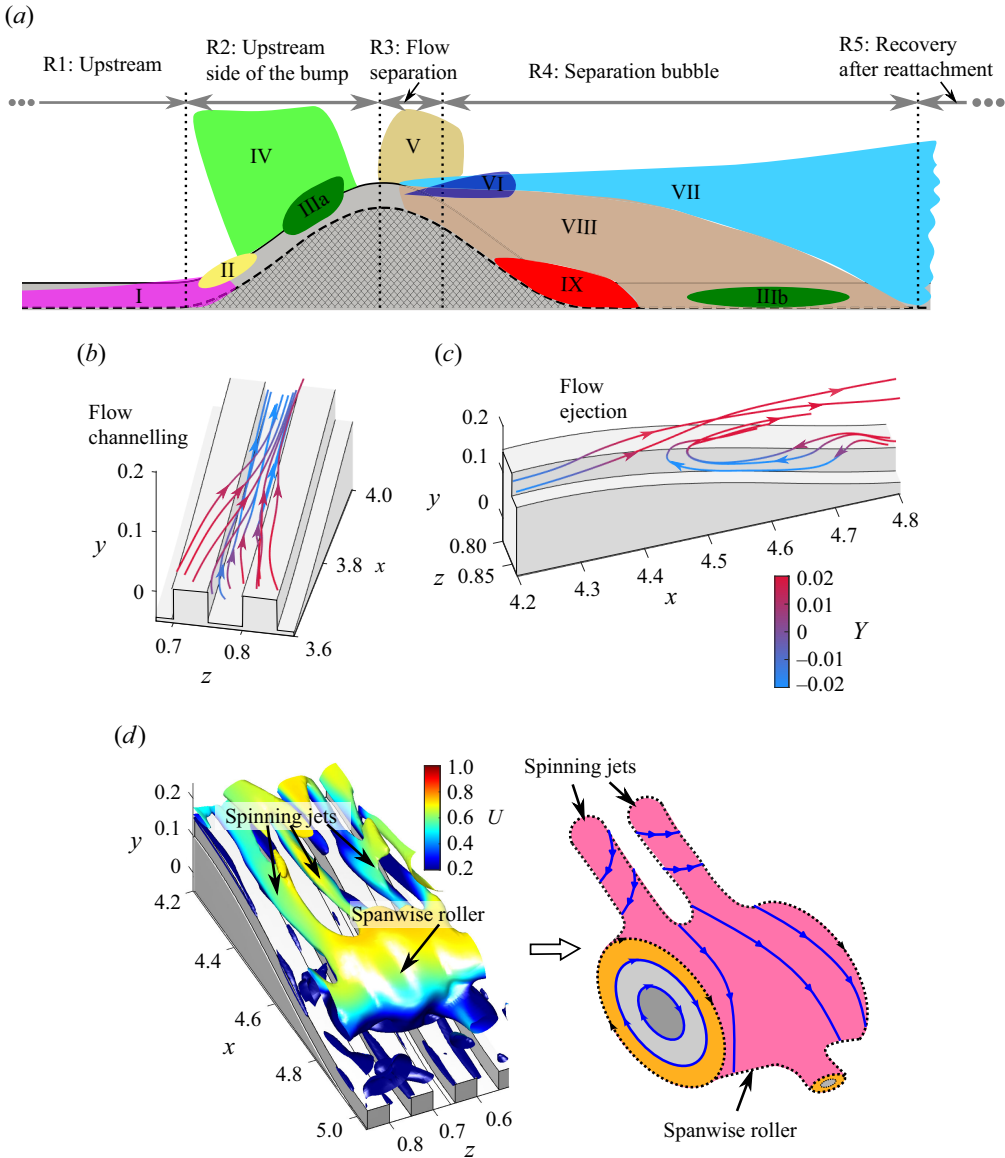


Figure 2. (a) Schematic denoting the regions of interest and important flow features as a summary of HGYS: I – upstream separation; II – incipient separation; IIIa,b – negative production; IV – FPG; V – APG; VI – spinning jets; VII – shear layer; VIII – SB; IX – minibubble. Isometric views of instantaneous streamlines over the GW showing (b) flow channelling into grooves and (c) flow ejection (lines are blue below the crest and red above). (d) Iso-surface of $-\lambda_2$ coloured by the streamwise velocity, U , and a sketch depicting the observed spinning jets and SR.

Inspection of the different contributions to turbulence production – shear stress production and normal stresses production – found that the decrease was predominantly in the normal stress production term, $-\langle u'u' \rangle \partial \langle U \rangle / \partial x$, and not from the shear stress production, $-\langle u'v' \rangle \partial \langle U \rangle / \partial y$. In HGYS, it was speculated that the counter-rotating spinning jets induced by the grooves extending into the shear layer and connecting with SRs (figure 2d) are responsible for the decrease in turbulence production. A distinct effect of the grooves

was to change the streamwise length of the downstream SB, increasing the reattachment length by more than 20 %. Since the spinning jets interact with SRs, the modified evolution of the rollers likely explains the extended mean reattachment, though no direct explanation was provided. Another significant effect of grooves is to increase the form drag of the bump by 25 % and decrease skin-friction drag by 5 % with respect to SW. Here, it is shown that changes in skin friction can be linked with the effect of grooves on the generation of minibubbles in the SB. Average negative production on the upstream side of the bump was observed and found to result from the streamwise normal stress production. In GW, an additional region of negative production was found inside the grooves also on the upstream side of the bump, the source being counter-gradient Reynolds shear stress in the shear production. By identifying nearby CSs, the role of CSs in these regions of negative production can be examined and compared with the expectation that CSs dominate energy production, even negative production.

2.4. Objectives

Flow statistics of the rich phenomena in a turbulent channel with a wall perturbation composed of a spanwise bump and longitudinal grooves were documented in HGYS, but are insufficient to provide the necessary insights into the flow physics. Here, we attempt to have a generalizable understanding of this flow, despite the specific geometry, by addressing the key flow statistics results summarized in § 2.3 via CS analysis. The changes in the peak turbulence intensity of the shear layer due to grooves are addressed first by acknowledging the SR as the dominant structure of this flow region. Coherent structure analyses are employed to quantify changes due to grooves in strength, size and evolutionary dynamics, such as conditional quadrant analysis, two-point correlations and phase-locked ensemble averages. Emphasis is laid on the modification of SRs by the CS – streamwise spinning jets – induced by the grooves and how the SB is subsequently influenced. Finally, the negative production observed in HGYS is explained by judicious inspection of instantaneous CS using the λ_2 criterion along with instantaneous vorticity and turbulence production for both SW and GW.

3. Instantaneous flow structures

Visualization of the flow field is important for grasping some details of CS; even a single realization sheds significant light. To better uncover the dominant vortical structures behind the bump, we examine the spanwise vorticity ($\Omega_z = \partial V/\partial x - \partial U/\partial y$) and λ_2 structures (Jeong & Hussain 1995) from the low-pass filtered velocity u_{L_i} using a Gaussian spatial filter with width equal to 0.05 in figures 3 and 4 and 0.1 in figure 5; the width of 0.05 provides a slight smoothing to improve clarity and 0.1, approximately the thickness of the shear layer at the location of peak turbulence intensity ($x \sim 5$), helps to uncover the SRs.

3.1. The Ω_z cross-section snapshots

The evolution of the most common flow features of the SW bump is shown through a sequence of Ω_z colour maps in x - y sections at an arbitrary z in figure 3. Past the bump peak, a shear layer emerges in some instances, extending significantly downstream without any immediate rollup of Ω_z (figure 3*a*). Interestingly, subsequent snapshots show that rollup happens simultaneously at different x locations (denoted by R in figure 3*b*) – this is atypical of all shear layers where rollup occurs sequentially, not simultaneously.

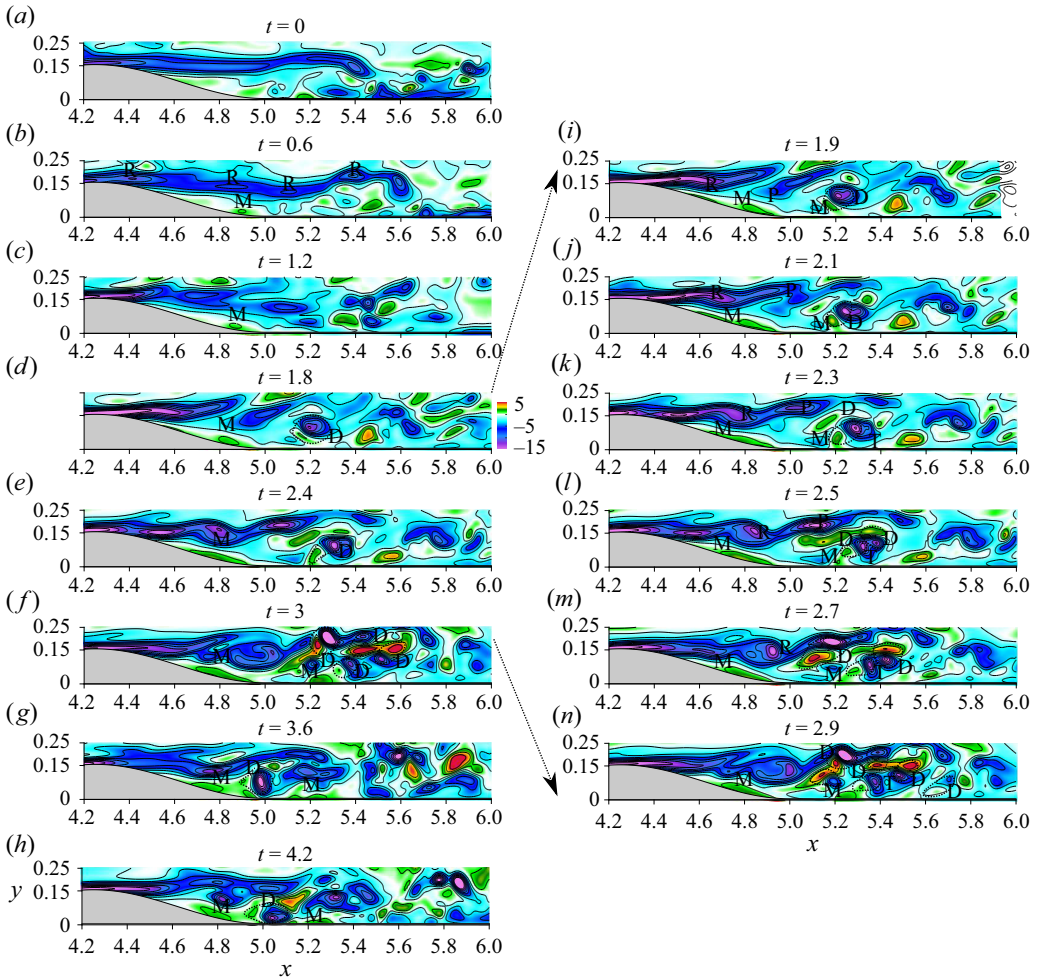


Figure 3. Smooth wall side-view sequence of instantaneous spanwise vorticity Ω_z from a low-pass filtered field (filter width $\Delta = 0.05$); the right column (*i–n*) with higher resolution in time from $t = 1.8$ to 3. The letter markers highlight different flow features: (M) secondary recirculation bubble (minibubble), (R) shear layer rollup, (P) vortex pairing, (D) vortex dipole and (T) vortex tearing. Further details of the flow between panels (*d*) and (*f*) are shown in panels (*i–n*), excluding panels (*d*), (*e*) and (*f*). Note that panel (*e*) is not repeated in the sequence (*i*) to (*n*).

Namely, the shear layer has characteristics of both a spatially developing shear layer and an only time-evolving shear layer. The rollup of the shear layer simultaneously at multiple x locations (although alike in a temporal mixing layer) is indeed rather striking and interesting and may involved coupling with the dynamics of the SB. This deserves careful study. Naturally, this flow features SRs pairing and tearing processes (P and T, respectively, in figure 3*i–n*), with associated frequencies discussed later concerning the SB unsteadiness. The shear layer vortices induce near-wall vortices of opposite sign due to the no-slip condition; these two vortices then combine to form a vortex dipole (two antiparallel vortices, henceforth called only dipole; D in figure 3*i,j*). The formation of dipoles is characteristic of this flow but is only observable from the instantaneous realization as it is a highly unsteady process and obviously hidden in the mean.

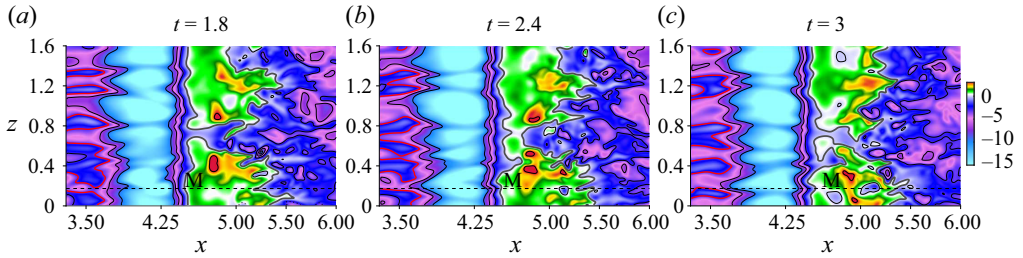


Figure 4. Smooth wall top-view sequence of spanwise vorticity Ω_z from a low-pass filtered field with filter size $\Delta = 0.05$ at $Y^+ = 1$. The dashed line denotes the z location for figure 3.

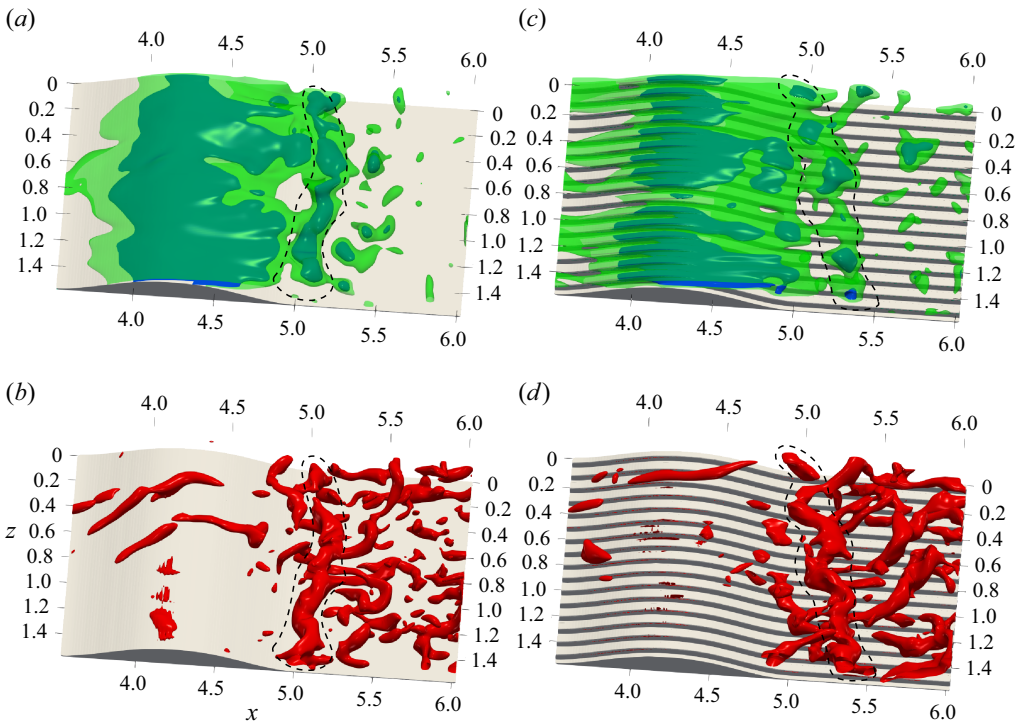


Figure 5. (a,c) Iso-surfaces of instantaneous spanwise vorticity ω_z and (b,d) iso-surfaces of λ_2 from a low-pass filtered field with filter size $\Delta = 0.1$. (a,b) SW and (c,d) GW. The dashed line in both the upper and lower figures indicates the underlying spanwise CS of interest.

3.2. Minibubble

Secondary recirculating regions – named ‘minibubbles’ in HGYS – attached to the wall are found in figure 3 (point M) around $x = 4.8$, identified by having $\Omega_z > 0$. As documented previously, the minibubble forms due to the streamline curvature of the near-wall upstream-moving flow of the SB and is not apparent in the mean flow for SW (note that the mechanism of minibubble formation is similar to that of the upstream flow separation); hence, it is interesting to see the instantaneous realizations and show its presence in SW. Furthermore, more than one minibubble can be observed at a time

(figure 3, points M), and in some instances, vorticity from a minibubble can be scooped up by the SRs to form dipoles (figure 3g,h,n). Note that, while minibubbles can lead to dipole formation, this formation does not require the presence of minibubbles. The motion of a minibubble is due to the combined influences of the SB's upstream flow near the wall and downstream advection of the minibubble due to its image vortex. The resulting advection is likely small, with no obvious direction of its motion.

Figure 4 shows the top views of Ω_z at $Y^+ = 1$ (a constant height above the wall and bump) to reveal the distribution of the minibubble in the z -direction. The minibubble can extend in the whole z domain, but more often is fragmented in z , as seen through the $\Omega_z > 0$ regions in figure 4(a,c). The grooves enhance coherence in the flow, always having a minibubble occurring at the grooves. The minibubble's coherence will be further discussed later through a CS analysis via the phase average of the SRs.

The flow features illustrated in figures 3 and 4 for SW are also observed in GW, thus examination of such snapshots is not repeated. Subsequent discussions will concentrate on the impact of grooves on these flow features, specifically through the incorporation of vortical structures that are directly associated with the grooves at the locations of flow separation.

3.3. The Ω_z and λ_2 structures

To better understand the three-dimensionality of the flow structures, figure 5 shows isometric views of Ω_z and λ_2 iso-surfaces. The prominent structures past the bump peak are SRs (denoted by dashed lines in each panel of figure 5) with z contortions – similar for both SW and GW. Such three-dimensionality emphasizes the need to carefully align CSs in a phase-average analysis – performed later – as even a single continuous structure varies significantly in z , such that different x - y planes of the same SR realization would reveal different features of the evolving CS.

The grooves become important near the bump peak, as discussed in HGYS. In particular, small-scale vortical structures with their axis aligned in the streamwise direction and attached to the crest corners of the grooves are observed in GW extending from the bump's peak into the shear layer. Figure 6 shows a sequence of zoomed-in views of the λ_2 structures (from the unfiltered field) behind the bump in the shear layer for SW and GW. The streamwise structures in GW weaken due to cross-diffusion as the streamwise vortices for a groove are counter-rotating, although some evidence of the streamwise structures remains on the SRs further downstream, as seen in figure 6(f). Thus, the grooves actively modify the SRs and the downstream flow dynamics. One objective of this study is to explain how the grooves' corner vortices affect the shear layer and SRs and, hence, flow separation.

3.4. Conceptual elucidation of the flow

For ease of discussion, the sketch in figure 7 highlights the relevant flow structures and dynamics we will analyse in detail. It shows the rollup of the shear layer, leading to the formation of SRs and the streamwise vortices (swirling jets) attached to the crests' corners. The separated region is below the shear layer up to the reattachment point. In addition, we accentuate the presence of vortex rods (the light blue structures in figure 7) at steep angles in the separated region, which are inferred in the next section to be more prevalent in GW, compared with SW, as well as flow structures that can be found within the SB such as secondary SBs (minibubbles) and vortex dipoles. Quasi-streamwise vortices in the region of accelerating flow upstream of the bump are found to be responsible for negative production and are discussed in § 7.

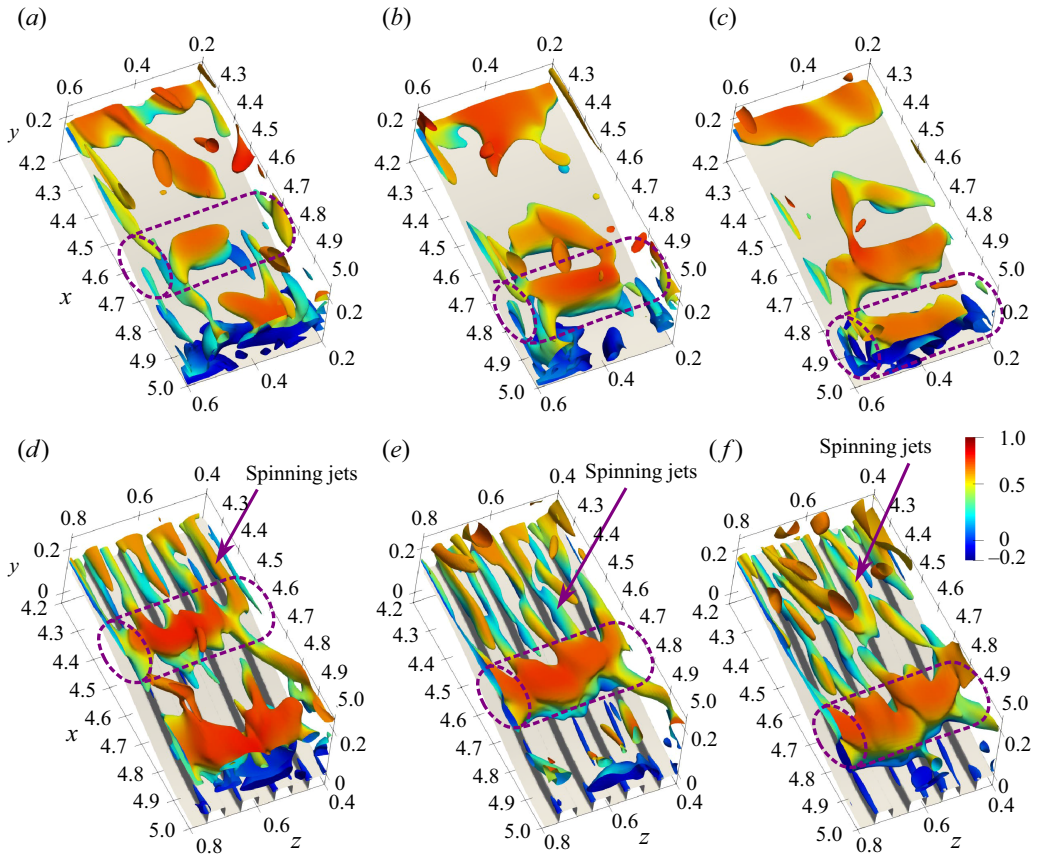


Figure 6. Sequence from left to right of a zoomed-in view of a subset of λ_2 -structures coloured by instantaneous streamwise velocity from an unfiltered velocity field: (a–c) SW; (d–f) GW. The dashed line in both the upper and lower figures indicates the underlying spanwise CS of interest. Note that separation occurs at $x = 4.4$ for both SW and GW. The SW reattachment is at $x = 5.38$, and GW reattachment is at $x \approx 5.49$.

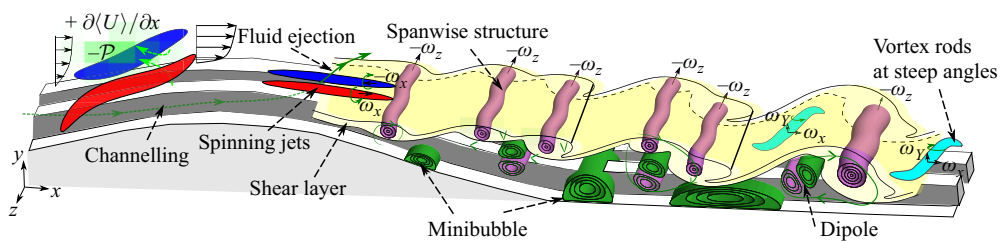


Figure 7. Schematic of the typical flow structure of the SB region with grooves. Conceptual elucidation of the organized flow.

4. Mean flow field

4.1. Quadrant analysis

In turbulent flows, coherent motions significantly contribute to the generation of the Reynolds shear stress (Lu & Willmarth 1973; Jeong *et al.* 1997; Schoppa & Hussain 2002),

which is directly connected to the turbulent momentum transport and, consequently, drag at the wall (Townsend 1976). The Reynolds shear stress can be divided into the contributions of quadrant events in the plane of streamwise and wall-normal fluctuations: Q1($u' > 0, v' > 0$) outward motions, Q2($u' < 0, v' > 0$) ejections, Q3($u' < 0, v' < 0$) inward motions and Q4($u' > 0, v' < 0$) sweeps (Wallace 2016). By understanding which quadrant Reynolds stresses are dominant in the various regions of the flow, one can then formulate the CS responsible.

Using the quadrant-splitting technique with the concept of the hyperbolic hole, the contribution from each quadrant and hole region can be defined as

$$\langle u'v' \rangle_{Q_i} = \frac{1}{N} \sum u'v' I_{Q_i}; \quad I_{Q_i} = \begin{cases} 1, & |u'v'| > \mathcal{H} \langle u'u' \rangle^{\frac{1}{2}} \langle v'v' \rangle^{\frac{1}{2}}; \quad (u', v') \text{ in } Q_i, \\ 0, & \text{otherwise,} \end{cases} \quad (4.1)$$

$$\langle u'v' \rangle_{\mathcal{H}} = \frac{1}{N} \sum u'v' I_{\mathcal{H}}; \quad I_{\mathcal{H}} = \begin{cases} 1, & |u'v'| \leq \mathcal{H} \langle u'u' \rangle^{\frac{1}{2}} \langle v'v' \rangle^{\frac{1}{2}}, \\ 0, & \text{otherwise,} \end{cases} \quad (4.2)$$

where N is the number of realizations, \mathcal{H} is the hole size and $\sum_{i=1}^4 \langle u'v' \rangle_{Q_i} + \langle u'v' \rangle_{\mathcal{H}}$ (Lu & Willmarth 1973). The hole size is chosen to be $\mathcal{H} = 3$ such that strong events, presumably associated with the large-scale and dynamically relevant CS, are captured. Previous investigations in flow separation (Krogstad & Skåre 1995; Schatzman & Thomas 2017) have shown that with $\mathcal{H} = 3$, Q2 and Q4 events dominate, while Q1 and Q3 make less than 1% fractional contribution to $\overline{u'v'}$. This dominance also holds for the zero-pressure-gradient TBL (without any separation) (Lu & Willmarth 1973); note that, for easy reference, we also use $\mathcal{H} = 3$ for the quadrant analysis. Moreover, Schatzman & Thomas (2017) showed that $\mathcal{H} = 3$ well captures the underlying shear instability and associated strong quadrant motions due to the coherent spanwise vorticity of SRs. A sample snapshot of $-u'v'$ in figure 8(j) shows that strong Q2 and Q4 events result from SRs. The claims below are not significantly affected by altering the threshold \mathcal{H} .

Consistent with that observed by Schatzman & Thomas (2017), we find that the peaks of $-\langle u'v' \rangle_{Q2}$ and $-\langle u'v' \rangle_{Q4}$ occur above and below, respectively, the inflection point ($\partial \overline{U} / \partial y = 0$) of the mean velocity (figure 8b,d,f,h) – with or without grooves. In agreement with HGYS, the Reynolds shear stress from strong sweep (Q4) and ejection (Q2) events decrease in magnitude in GW. Hence, if one considers Q2 and Q4 events a direct result of the SRs, the rollers in GW are ‘weaker’ in generating Reynolds shear stress.

The effect of grooves is further detailed through the profiles of quadrant Reynolds shear stress where $-\langle u'v' \rangle_{Q4}$ is significantly suppressed – much more than $-\langle u'v' \rangle_{Q2}$ – near the wall at the onset of the shear layer (figure 8i at $x = 4.5$). This suppression is attributed to the fluid ejection promoted by grooves that inhibit the sweep motion. Specifically, a sweep motion below the shear layer – with a $-v'$ fluctuation – is countered by the fluid jetting from grooves. Additionally, the profiles in figure 8(i) show a vertical shift of the inflection point (shear layer) away from the wall in GW due to the fluid ejection introduced by grooves at the onset of the shear layer, an aspect previously pointed out in HGYS. The average height of the inflection point is $y = 0.143$ for SW and $y = 0.158$ for GW with minimal streamwise variation from $x = 4.5$ to 5.5. These results provide initial insights into the effect of grooves on the SRs, showing that changes in the Reynolds shear stress are due to modification of the SRs. Through the CS analysis later in § 5, we further detail the relation of the Reynolds shear stress uncovered with the quadrant-splitting technique and the SRs.

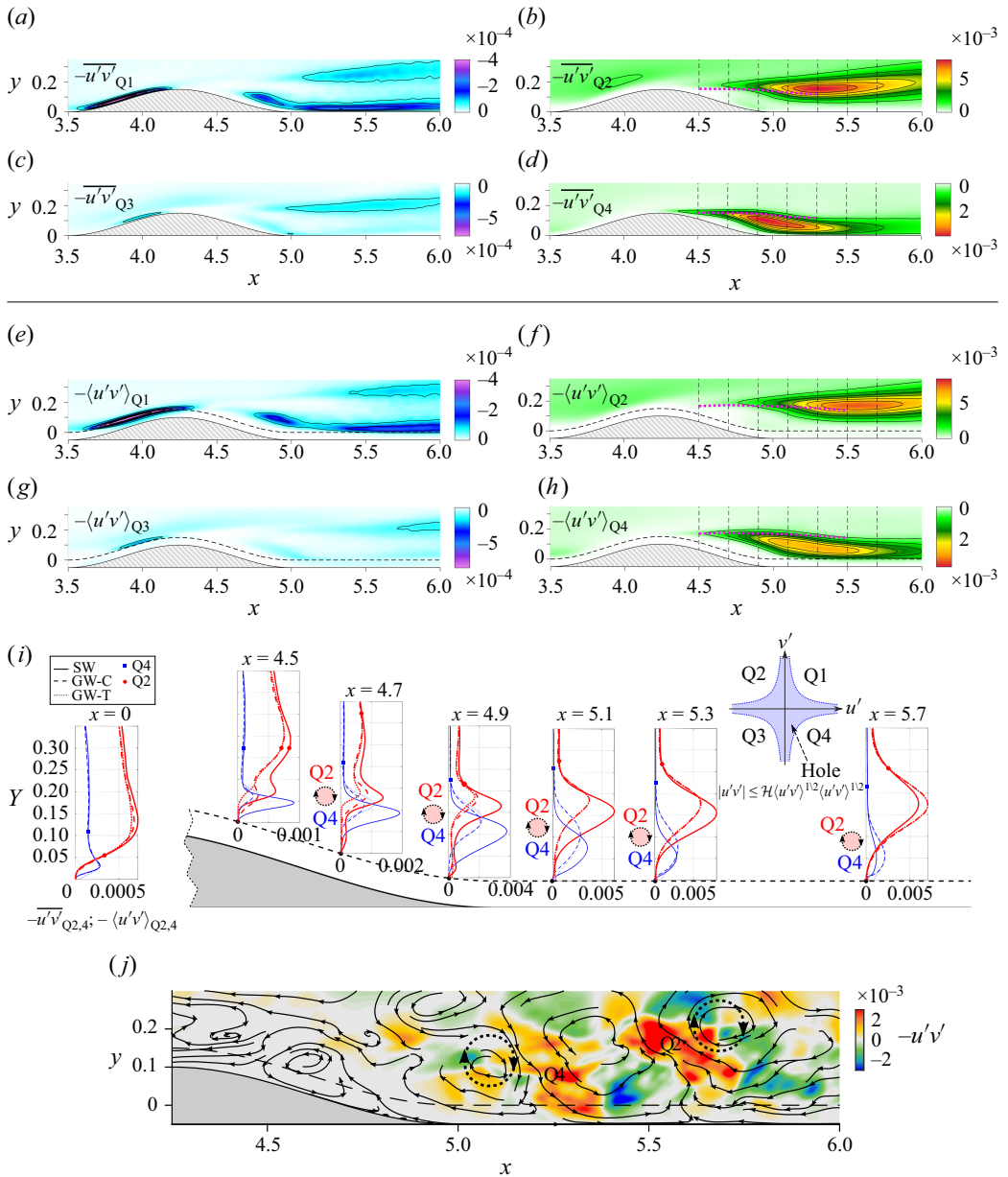


Figure 8. Colour maps of quadrant Reynolds shear stress in x - y section with $\mathcal{H} = 3$. Panels show (a-d) SW, $-\overline{u'v'}_{Q_i}$; (e-h) GW at the centre of grooves, $-\overline{u'v'}_{Q_i}$. The dotted line denotes the inflection point of the mean velocity profile. (i) Profiles of Q2 and Q4 Reynolds stresses at different streamwise locations for SW, GW at the centre of crests (GW-C), and GW at the centre of groove troughs (GW-T); approximate locations of the CS responsible for Reynolds stresses are shown as dashed circles with the direction of velocity corresponding to the quadrant. For (e-i), the dashed line indicates the crest height position. (j) Sample snapshot of Reynolds shear stress events Q2 and Q4 superimposed with streamlines projected into the x - y plane.

As a side note, we showed in HGYS that negative Reynolds shear stress occurs on the upstream face of the bump. Figure 8(a,c) emphasizes that this is a consequence of the increased Q1 events as the flow is accelerated by the bump, narrowing the channel area. On the other hand, the Q3 events are negligible throughout the channel, for cases with or without grooves (figure 8e,g).

4.2. Two-point correlations

A consistent swirling motion at a specific position may appear in space as regions of highly correlated velocity fluctuations – providing statistical information about their geometrical characteristics. In this section, we examine the statistical characteristics of CS based on the two-point correlations of velocity and pressure fluctuations.

The generic two-point correlation is defined as

$$r_{\phi\phi}(x_0, y_0, z_0, \Delta x, \Delta y, \Delta z) = \frac{\langle \phi'(x_0 + \Delta x, y_0 + \Delta y, z_0 + \Delta z, t) \phi'(x_0, y_0, z_0, t) \rangle}{\langle \phi' \phi' \rangle^{\frac{1}{2}}(x_0, y_0, z_0) \langle \phi' \phi' \rangle^{\frac{1}{2}}(x, y, z)}, \quad (4.3)$$

where coordinate (x_0, y_0, z_0) is the reference point and ϕ can be any independent variable of the flow (i.e. velocity, pressure, etc.). Note that the two-point correlations are averaged in the z -periodic direction over all grooves at the same relative positions, i.e. z_0 is a reference point to the span groove's wavelength (λ_g), and in SW, the two-point correlations are not a function of z_0 .

4.2.1. Velocity correlations

A comparison of the 3-D correlation structure (correlation iso-surface) obtained for the velocity fluctuations for a flat SW, the SW and the GW bumps is provided in figure 9. The r_{uu} iso-surfaces for the flat SW with reference point $y_0 = 0.12$ ($y_0^+ = 36$) (figure 9a) appear to be very elongated in the x -direction with a length of approximately $\Delta x^+ = 10^3$ – a result due to the near-wall streaks observed in the buffer layer (Jiménez 2013; Sillero, Jiménez & Moser 2014). The r_{uu} iso-surfaces for the SW bump – with the reference point x_0 taken above the recirculation bubble where root-mean-square (r.m.s.) of pressure fluctuations (p_{rms}) is maximum – are similarly streamwise elongated to that over the flat SW; however, the length is 60 % of that of the flat SW (using $r = +0.2$). This is consistent with the findings in HGYS that the streaks are suppressed above the recirculation bubble. Different from the flat SW, the inclination angle of the positive lobe is negative in the xy plane (figure 9d), which is expected as r_{uu} depicts u' -structures in the reattaching shear layer behind the bump. Moreover, the negative r_{uu} lobes are more pronounced and at the same distance from the wall as that for positive r_{uu} lobe – different from the case in the flat wall which are at the wall – indicative of the r_{uu} iso-surfaces describing structures predominantly on the shear layer. For GW, r_{uu} iso-surfaces are no longer elongated in the x -direction, consistent with the observation in HGYS that the flow becomes more isotropic with grooves. The negative r_{uu} lobes in GW (figure 9g) appear to be more rod-like than in SW (figure 9d), with a steeper angle in the xy plane, which is linked with the more marked presence of vortex rods at steep angles when analysed together with r_{ww} (detailed below). In GW, the r_{uu} iso-surfaces appear to be disconnected from the bump peak highlighting the disrupted shear layer by the presence of streamwise structures favouring v' and w' velocity fluctuations.

The two-point correlations of cross-flow velocity fluctuations (r_{vv} and r_{ww}) for the flat SW case (figure 9b,c) are associated with the quasi-streamwise vortices in the buffer layer (Jiménez 2018). The effect of the bump modifies this interpretation significantly,

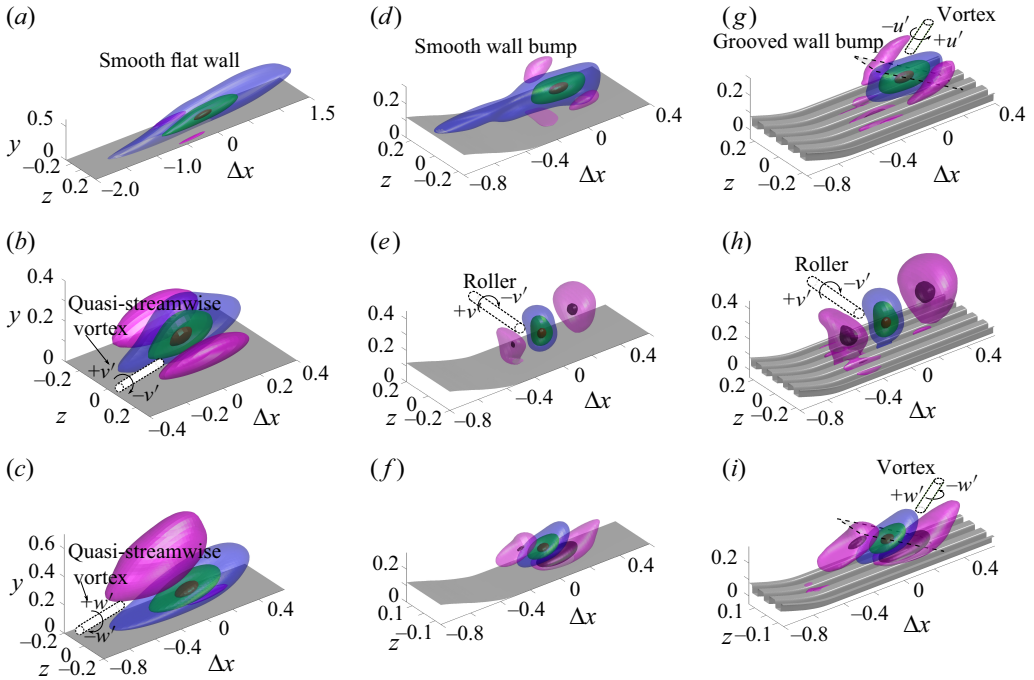


Figure 9. Three-dimensional iso-surfaces of two-point correlations of the three velocity components for (a–c) the flat SW, (d–f) SW bump and (g–i) GW bump. Panels show (a,d,g) r_{uu} ; (b,e,h) r_{vv} ; (c,f,i) r_{ww} . Iso-surfaces are $r = +0.8$ (red), $r = +0.4$ (green), $r = +0.2$ (blue), $r = -0.1$ (magenta) and $r = -0.2$ (black). The reference point for the flat wall is $y_0 = 0.12$ ($y_0^+ = 36$), for the bump cases are the point of peak r.m.s. pressure fluctuations: SW at $(x_0, y_0) = (5.2, 0.12)$ and GW $(5.47, 0.134)$ at the centre of troughs. Quasi-streamwise vortices and SRs responsible for the correlated velocities are sketched in (b,c,e,g,h,i) for reference.

particularly for r_{vv} (figure 9e). The negative r_{vv} lobes appear upstream and downstream of the positive correlation lobe instead of being located on the sides (in the z -direction) as in the flat SW case. Clearly, the presence of SRs is responsible for the distribution of r_{vv} as they induce $+v'$ and $-v'$ motions in the back and front as they move downstream above the SB, causing r_{vv} to change sign in the x -direction. Similar r_{vv} surfaces are observed for GW (figure 9h); however, the $r_{vv} = -0.2$ iso-surfaces are larger and overall more symmetric in the x -direction, i.e. the negative lobes are of the same size and same distance with respect x_0 – perhaps because of a more matured SR as x_0 is slightly further downstream. The r_{ww} iso-surfaces for the bump cases (with or without grooves, figure 9f,i) are similar to those of the flat SW (figure 9c); namely, the negative–positive–negative r_{ww} lobes are stacked in the x – y plane. Not surprisingly, the r_{ww} iso-surfaces do not show any indication of SRs, as SRs mostly induce u' and v' .

An interesting observation is that r_{uu} and r_{ww} in GW, if examined together, can be interpreted to be the result of a vortex rod at a steep angle in the xy plane. For reference, figure 10(a,b) shows the r_{uu} and r_{ww} contours extracted on a plane that is 30° with respect to the $-x$ direction for GW (figure 9g,i). The contours of r_{uu} and r_{ww} support the presence of a vortex rod (indicated by the green-shaded circle), idealized in the sketch in figure 10(c), which would produce such velocity correlations. Therefore, GW is perhaps more notably populated by vortex rods at steep angles past the bump perturbation. Further

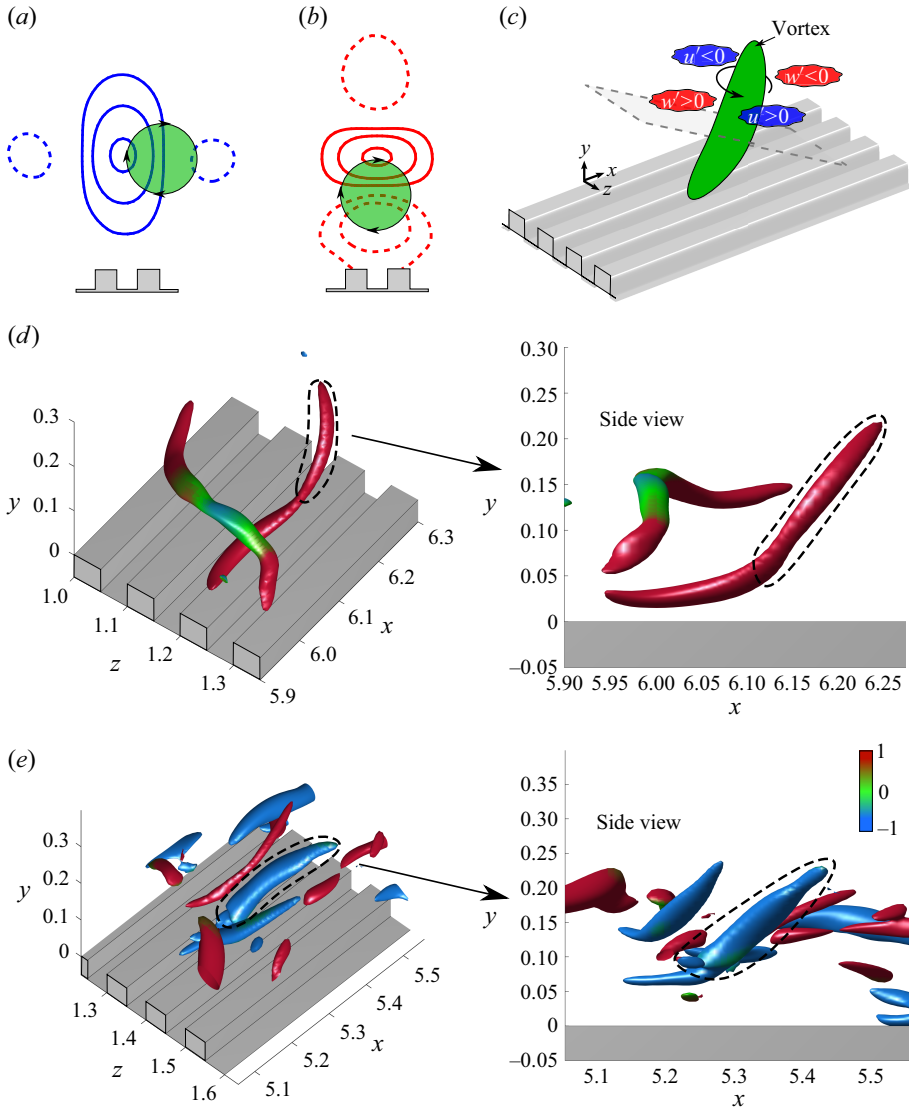


Figure 10. Two-point correlation contours of (a) streamwise velocity fluctuations r_{uu} and (b) spanwise velocity fluctuations r_{ww} in the planar section denoted in figure 9(g,i) with 30° in the $x y$ plane with the horizontal. Solid lines indicate positive correlations, and dashed lines negative. (c) Sketch of a vortical structure that would produce the present r_{uu} and r_{ww} , with blue and red corresponding to the contours in (a) and (b), respectively. Note that the green circle in (a) and (b) corresponds to a slice through the CS in (c). (d,e) Instantaneous realizations of λ_2 -structures for GW coloured by ω_x , with dashed lines indicating the λ_2 structures of interest.

evidence to elaborate this speculation is provided in figure 10(d,e), where instantaneous λ_2 -structures at high angles are found within the separated flow region.

4.2.2. Pressure correlations

As vortices are expected to have low-pressure regions within their core (Jeong & Hussain 1995), the correlation of the (fluctuating) pressure field (p') can also be used as an

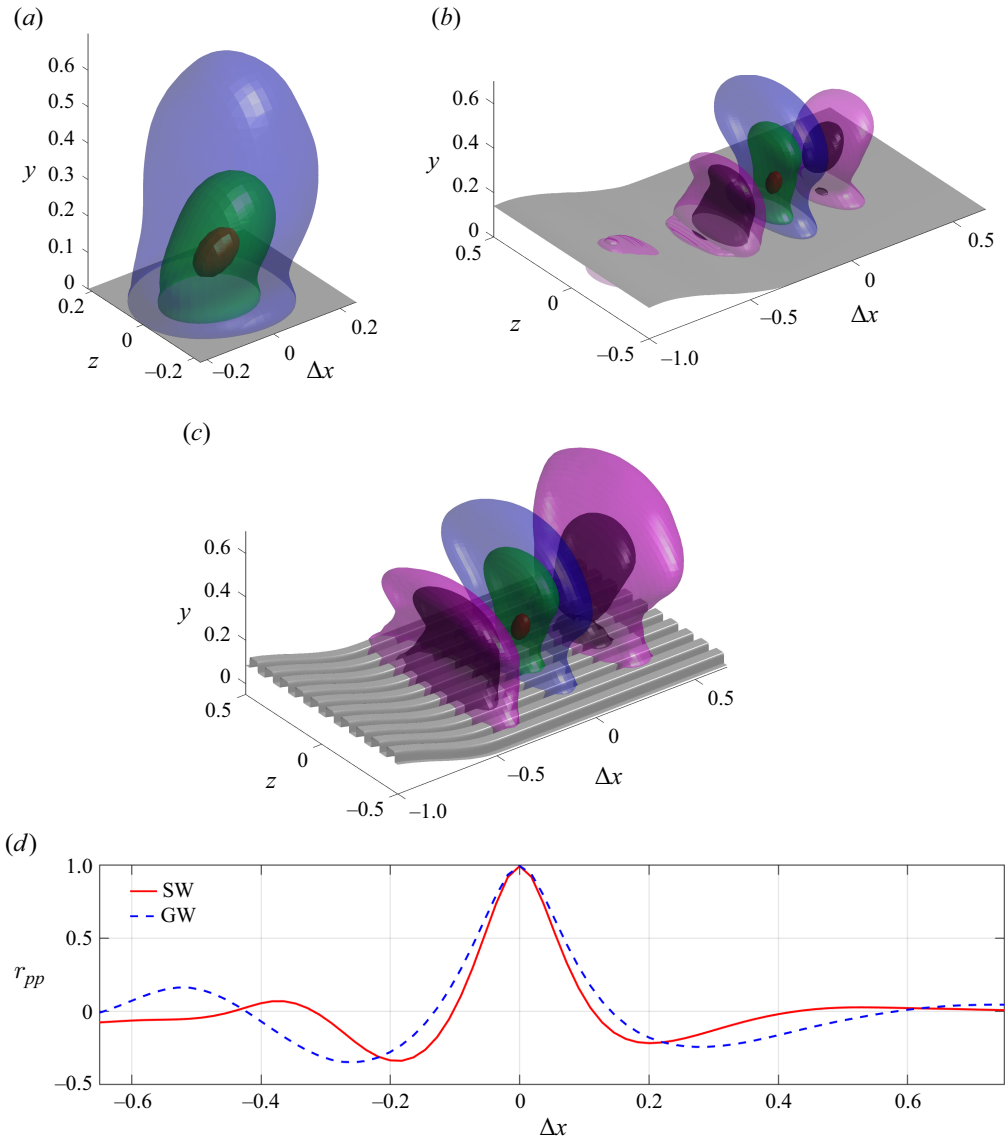


Figure 11. Three-dimensional iso-surfaces of two-point correlations for pressure fluctuations. (a) The flat SW, (b) the SW bump and (c) the GW bump. The reference point for the flat wall is $y_0 = 0.12$ ($y_0^+ = 36$), for the bump cases are the point of peak r.m.s. pressure fluctuations: SW at $(x_0, y_0) = (5.2, 0.12)$ and GW $(5.47, 0.134)$ at the centre of troughs. (d) Profiles of r_{pp} as a function of streamwise increment Δx at y_0 for SW and GW.

indication of the CS spatial distribution. For the flat SW, the r_{pp} surfaces (figure 11a) are approximately circular in the $x-z$ plane and extend significantly in the y -direction (Kim 1989). The bump perturbation causes significant modifications in r_{pp} (figure 11b), with the overall distribution resembling r_{vv} (figure 9e). The r_{pp} iso-surfaces capture the low pressure of SRs even when they are contorted in z by showing a larger extent of r_{pp} in z . Outside the vortex, the correlation of the random velocity fluctuations of the turbulent SR will be weaker than that of pressure. Hence, pressure footprint of a SR will have higher spanwise correlation than of wall-normal velocity. The iso-surfaces of r_{pp} for the GW case

extend more in the z -direction than those for the SW case – suggesting that the SRs are more coherent along that direction. More quantitative information of the effect of grooves on the SRs can be obtained by looking at the streamwise profile of r_{pp} (figure 11*d*). The distance between local maxima, which represents the spacing between consecutive SRs, increases for the GW case. This suggests that the rollup frequency of the SRs decreases – an observation confirmed in § 6 via spectral analysis.

5. Coherent structure analysis

We focus here on the effect of grooves on the dynamics of the most prevalent CS (i.e. the SRs) generated by the bump perturbation. Particular attention will be given to the alteration of the flow dynamics promoted by flow ejection, as well as the associated corner vortices on the SRs and their evolution for GW. The following analysis employs the vorticity-based eduction method developed by Hussain (1986).

5.1. Phase-locked ensemble averaging of CS

The eduction of the CS is both sophisticated and elaborate. The interest here is to educe the dominant spanwise CS present in the shear layer, as visualized in Muller & Gyr (2020) and conceptually described in Muller & Gyr (1986). For this purpose, a visual inspection of the instantaneous structures in an x - y plane is performed using the instantaneous spanwise vorticity (Ω_z) and $-\lambda_2$. For example, figure 12(*a,b*) shows the Ω_z and $-\lambda_2$ colour maps obtained from an arbitrary time and z position for SW. Note that, at this particular instant, ω_z resembles pairing as described in Hussain & Zaman (1980); however, the $-\lambda_2$ shows a single peak in the centre.

To characterize the dominant spanwise structures, a local time-dependent circulation parameter is computed as

$$\gamma = \int \Omega_z dA, \quad (5.1)$$

over a squared region across the shear layer; figure 12(*c*) shows the evolution of γ for the red square box in figure 12(*a,b*). Note that the side length of the box in figure 12(*b*) is 0.1, which, as mentioned earlier, is approximately the thickness of the mean shear layer. For any selected x location, there is smearing of the educed structure in y if we do not bound in the y direction due to jitter between successive passing structures as well as random spanwise waviness of the SRs. Hence, both x and y locations of the point of eduction (squared box) must be precisely selected *a priori*; therefore, only a small fraction of the total structures will be used for eduction. The phase average considers only strong events where γ has a local negative peak below one standard deviation past the mean γ (denoted by the shaded region below the dash line in figure 12(*c*)). The snapshot in figure 12(*a,b*), which corresponds to the time marked by the filled red circle in figure 12(*c*), exemplifies that the negative peaks of γ correspond to SRs. The criterion for choosing instantaneous realizations based on the time series of γ is used for the first estimate ensemble average (zeroth ensemble) with the following two additional conditions: (i) a local peak of $-\lambda_2 > 0$ must exist in the red square of figure 12(*b*); and (ii) the vorticity vector at the peak of $-\lambda_2$ must be within a cone of 30° along the $-z$ direction. These criteria resulted in only ~ 600 structures being considered for eduction sifted out of millions of structures; this necessarily requires a very long simulation.

Following Hussain & Hayakawa (1987) the ensemble average is obtained by phase aligning the structures through a time shift to increase the cross-correlation of Ω_z in the

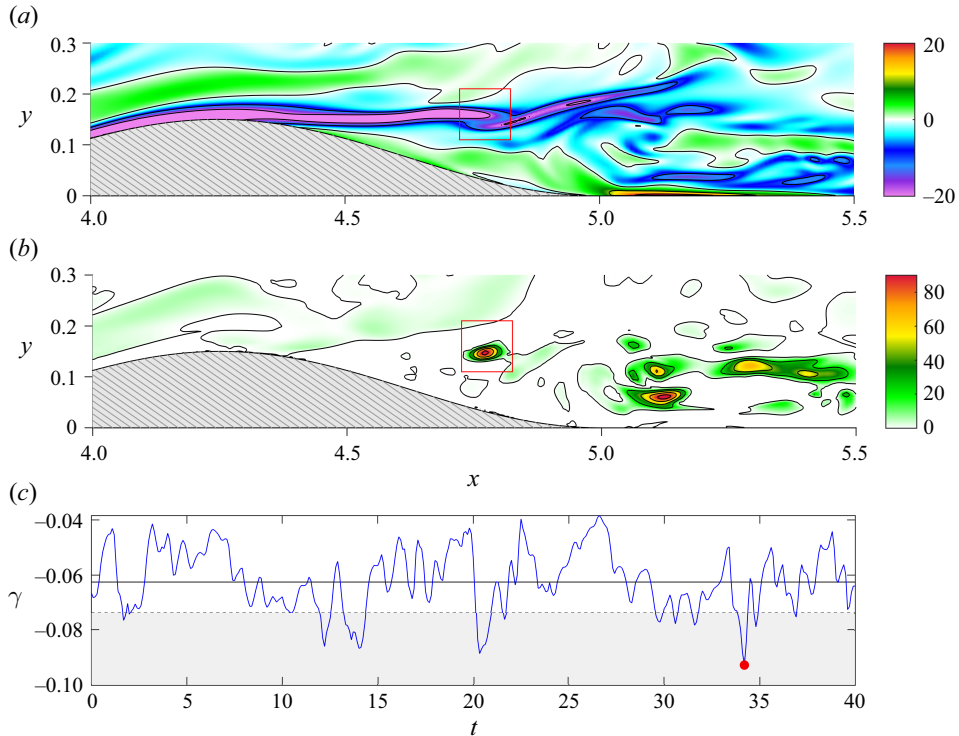


Figure 12. Colour maps of instantaneous (a) spanwise vorticity, ω_z , and (b) vortex identification criterion, $-\lambda_2$, in an xy section at an arbitrary spanwise position. (c) Time series of a local circulation, γ , computed for the red square in (a,b); the colour maps in (a) and (b) correspond to the time highlighted by the red filled circle in (c). The solid line denotes the mean value of γ , the dashed line denotes the standard deviation of γ and the grey shaded region corresponds to the values of γ considered.

squared region chosen. A realization is discarded if the correlation coefficient with the ensemble average is lower than a specified value R_t , defined as

$$R_t = \frac{1}{2N} \sum_{i=1}^N R_i. \quad (5.2)$$

Here, R_i is the correlation value for the i th realization, and N is the total number of realizations being considered for the new ensemble average. The process is iterated by replacing the zeroth ensemble with the latest ensemble until no more realizations are removed from the considered ensemble. The phase-averaging procedure is performed at different stations with coordinates corresponding to the centre of the square box at $(x, y) = \{(4.7, 0.16), (4.85, 0.16), (5, 0.16), (5.2, 0.12), (5.47, 0.13)\}$. The coordinates are arbitrarily chosen: the first three stations centred at the shear layer, and the second-last and last stations at the peak of p_{rms} for SW and GW, respectively. For both SW and GW, the final phase averages are obtained using ~ 250 structures at each station.

5.2. Coherent structure measures

5.2.1. Educed vortical structures

The phase averaging procedure to educe SRs in the shear layer was performed at five different phases of the evolution of the SRs (we call them stations), moving downstream

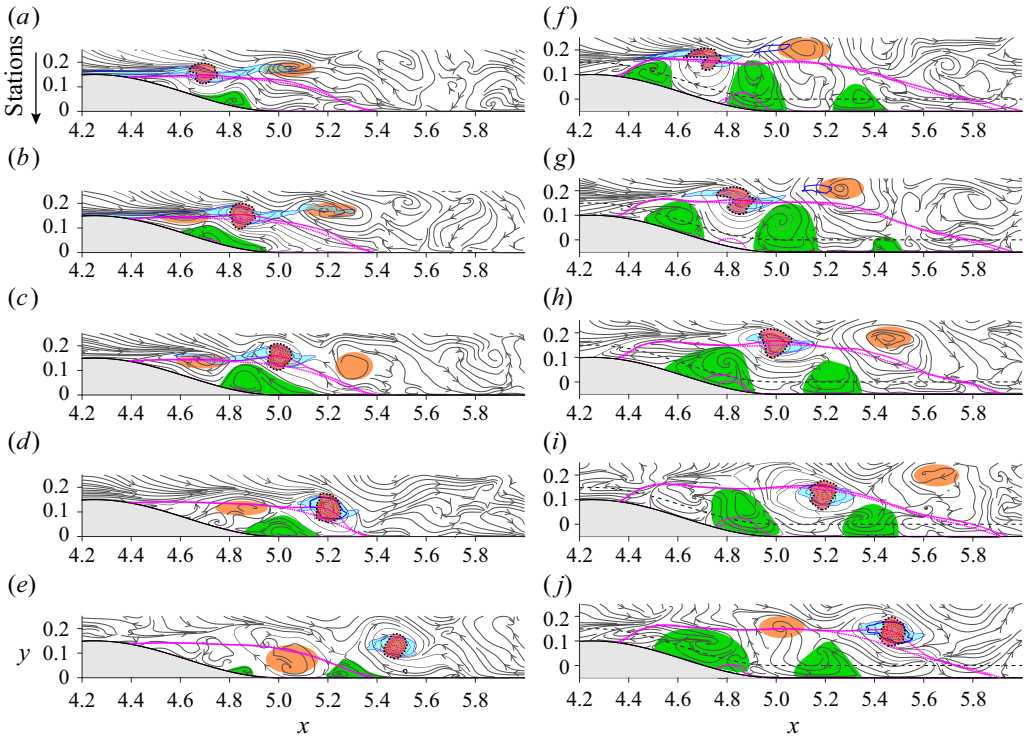


Figure 13. Contours of $-\lambda_2(\partial[U_i]/\partial x_j)=0.5, 3, 5.5, 8$ (red dotted line) at different stations from top to bottom superimposed with the coherent streamlines (\bar{u}, \bar{v}) , contours of $\tilde{\omega}_z = -1.3, -2.3$ (blue lines), the phase-average $([U], [V])$ dividing streamline (magenta solid line) and time-averaged dividing streamline (magenta dotted line) for (a–e) SW, and (f–j) GW at the centre of grooves. The eduction locations (the red contour centres) are arbitrarily chosen – the same for SW and GW. The red patches identify the educed SRs, the yellow patches denote nearby SRs and the green patches the near-wall minibubbles. Both the yellow and green are unavoidably smeared due to the inherent jitter with respect to the educed red structures.

up to the peak p_{rms} (figure 13). In the case of SW, the peak of p_{rms} is earlier than that in GW, but for completeness, we include for SW the station where the peak p_{rms} occurs for GW. In SW for stations at $x = 4.7, 4.85$ and 5 , we see that $\tilde{\omega}_z$ (for the threshold chosen) depicts a shear layer and not closed circular loops, although a well-defined SR structure is obtained from λ_2 of the phase-averaged field (figure 13a–c,f–d). In the early stages of the rollup process, the shear layer is constant and steady and, therefore, emerges in the phase average. As the roller matures moving downstream, the contours of $\tilde{\omega}_z$ become circular – like λ_2 – and clearly identify the SR as a separate structure from the shear layer. The effect of groove spinning jets is evident in altering $\tilde{\omega}_z$ by breaking the coherence of the shear layer in the early stages of the formation of SRs. The fact that $\tilde{\omega}_z$ does not have a well-established shear layer in GW may indicate that the rollup process is being delayed, hence this is evidence of the delayed peak of turbulence and the changes to $-\langle u'u' \rangle \partial \langle U \rangle / \partial x$ seen by HGYS.

Interestingly, in the coherent velocity field, minibubbles are found embedded within the large SB on the downstream side of the bump. The fact that the eduction of SRs always captures minibubbles implies spatial coherence between the minibubble and SRs. Such spatial coherence is enhanced by the induction of the image vortices. The minibubble is influenced by the shear layer rollup but is also subjected to the induction of the image,

the combined effect would be an interesting study. Here, the mean field is indirectly represented by the phase-average dividing streamline (purple lines in figure 13*a–j*) with no evidence of the minibubble for SW (figure 13*a–e*) in contrast to GW, which shows the minibubble within grooves at $x \approx 4.8$ in figure 13(*h–j*). The effect of grooves is to enhance the extent and prevalence of the minibubble in the coherent velocity within the SB (figure 13*f–j*). Here, we understand why the minibubble also appears in the mean flow for GW as it is more dominant and frequent in the coherent flow, always having a footprint at $x = 4.8$ inside the grooves. Note that in GW, for the early stages of the SR, there are three simultaneous minibubbles versus only one in SW. In HGYS, we observed lower skin friction in GW compared with SW near the downstream end of the bump (around $x = 5$), where near-wall flow is moving upstream. The lower skin friction could be attributed to the minibubbles deflecting the upstream-moving flow away from the wall, leading to a reduced time-average skin friction there. Moreover, the minibubbles contribute to skin friction because the velocity underneath them is downstream – further compounded by its image vortex. These three effects – deflection of the SB flow by the minibubble away from the wall, the minibubble bottom flow downstream and the effect of the image vortex – combine together to alter the skin friction and form drag in this region.

5.2.2. Coherent Reynolds shear stress

In the early stage of the SR in SW (figure 14*a* at $x = 4.7$), the coherent Reynolds shear stress is dominated by Q4 sweep events and Q3 inward motions, while the Q2 ejections and Q1 outward motions are inhibited, perhaps expected because the upstream half of the SR is closer to the wall and bump peak, i.e. the SR is not yet well developed and the upstream half is very close to the onset of the shear layer. A cloverleaf-like pattern in $-\tilde{u}\tilde{v}$ is formed at $x = 4.85$ (figure 14*a*), similar to SRs found in mixing layers (Hussain & Zaman 1980; Hussain & Hayakawa 1987). In GW, the cloverleaf pattern $-\tilde{u}\tilde{v}$ is delayed, indicating the disruption of the rollup of $-\Omega_z$ due to the presence of grooves inducing a series of swirling jets at the point of separation near the bump peak. The cloverleaf patterns for both SW and GW are not exactly axisymmetric; therefore, on average, they make some (positive) contribution to the total (time-averaged) Reynolds shear stress. If the structure cross-section is circular (in the x - y plane), the four lobes will be equal (figure 14*d*). For an elliptic SR where the lobes from each axis are distinct from each other, the spatial distribution of $-\tilde{u}\tilde{v}$ has regions of both positive and negative values, and which sign dominates in the time average depends on the orientation of the SR. The sketch in figure 14(*d*) shows the effect of the inclination of an elliptic SR; the peak of $-\tilde{u}\tilde{v}$ is positive if the SR is inclined toward the wall, and otherwise, if it inclines away from the wall. Here, we see that $-\tilde{u}\tilde{v}$ always makes a positive contribution to $-\langle u'v' \rangle$ throughout the evolution of SRs for both SW and GW as the educed structure is always elliptic and with an inclination toward the wall – perhaps characteristic of SRs in the shear layer above a SB. The peak of $-\tilde{u}\tilde{v}$ oscillates between Q2 and Q4 events for the five stations analysed. The limited thickness of the bubble and the limited length of the shear layer together prevent the typical tumbling of the SRs. This contrasts a typical mixing layer in which the SRs would tumble, varying their geometry among the three shapes in figure 14(*d*) occurring randomly in space and time – resulting in a net zero contribution to the time-averaged Reynolds shear stress; the net zero Reynolds stress results not only from the symmetric but also from the tilted structures occurring randomly in space and time (Zaman & Hussain 1980).

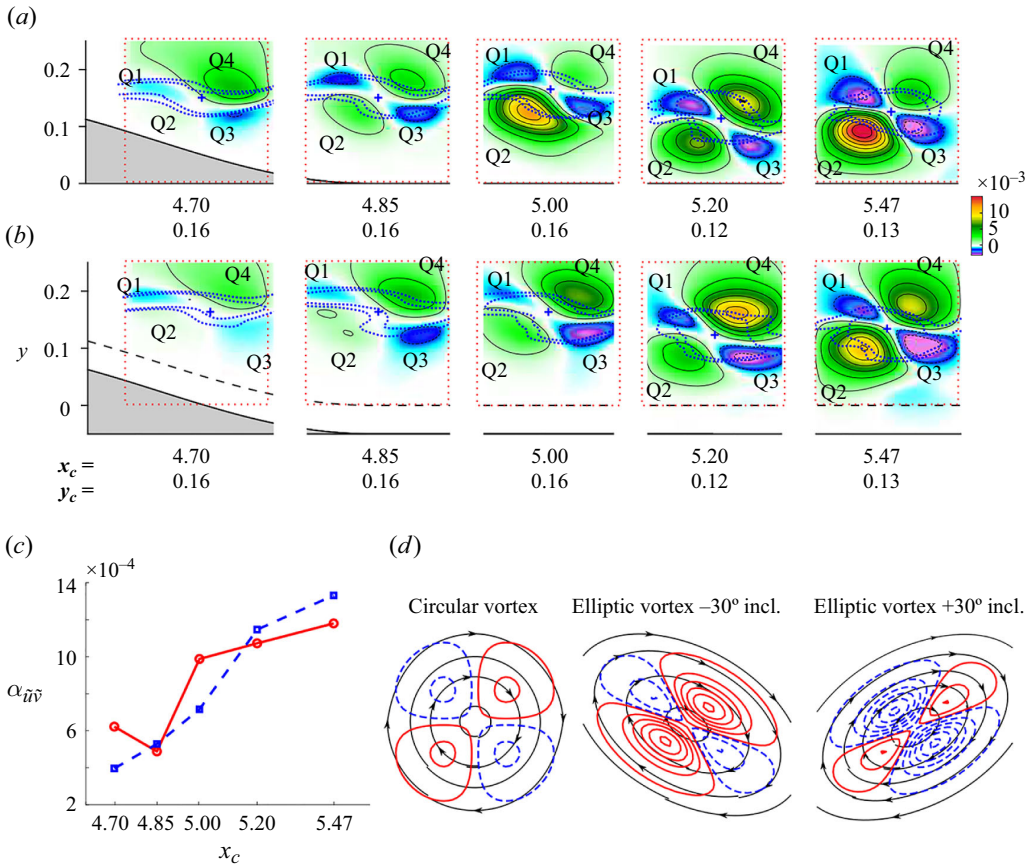


Figure 14. Coherent Reynolds shear stress $-\tilde{u}\tilde{v}$ at different x -stations superimposed with contours of $\tilde{\omega}_z$ at levels $-2.3, -1.3$ (red dotted lines) for (a) SW, and (b) GW at the centre of grooves. Here, x_c and y_c denote the (x, y) locations of the centres for eduction in each panel. Panel (c) shows the $-\tilde{u}\tilde{v}$ area average over the dotted squares in (a,b), $\alpha_{\tilde{u}\tilde{v}} = A_{square}^{-1} \iint -\tilde{u}\tilde{v} dx dy$; solid line SW and dashed line GW. (d) Sketch comparing the coherent Reynolds shear stress distributions of CS of different cross-sections: a circular SR, an elliptical SR inclined upstream and downstream (solid line positive values and dashed lines negative values). In (a,b), a + sign identifies the location for eduction alignment and is very close to the location of $\tilde{\omega}_z$ peak; Q1, Q2, Q3, and Q4 identify the quadrants, and the x -range of each panel is 0.2.

5.2.3. Coherent and incoherent productions

When examining the coherent production (production of coherent motion by mean shear), $\mathcal{P}_c = -\tilde{u}_i \tilde{u}_j \langle S_{ij} \rangle$, where $S_{ij} = (\partial U_i / \partial x_j + \partial U_j / \partial x_i) / 2$ (figure 15a,b), we obtain a cloverleaf pattern similar to that in $-\tilde{u}\tilde{v}$, indicating that $-\tilde{u}\tilde{v} \langle S_{12} \rangle$ is the dominant contribution to \mathcal{P}_c – but of course with different peak values. The coherent Reynolds stress for both SW and GW are increasing up to the last station measured (figure 13c), while the maximum \mathcal{P}_c values occur at $x_c = 5$ (SW) and $x_c = 5.2$ (GW). The peak values of \mathcal{P}_c occur before the peaks of production ($-\overline{u_i u_j} \overline{S_{ij}}$ in SW; $-\langle u'_i u'_j \rangle \langle S_{ij} \rangle$ in GW) at $x_c = 5.2$ and $x_c = 5.47$ for SW and GW, respectively (see HGYS). The shear action in producing coherent motion is maximum prior to the point of breakup of the SRs (on average), which is where the peak of production and dissipation is to be expected.

The incoherent (random) turbulence intensity, $[u''u'']$, is similar to the (time average) turbulence intensity, $\langle u''u'' \rangle$, reported by HGYS – increasing with x past the bump peak

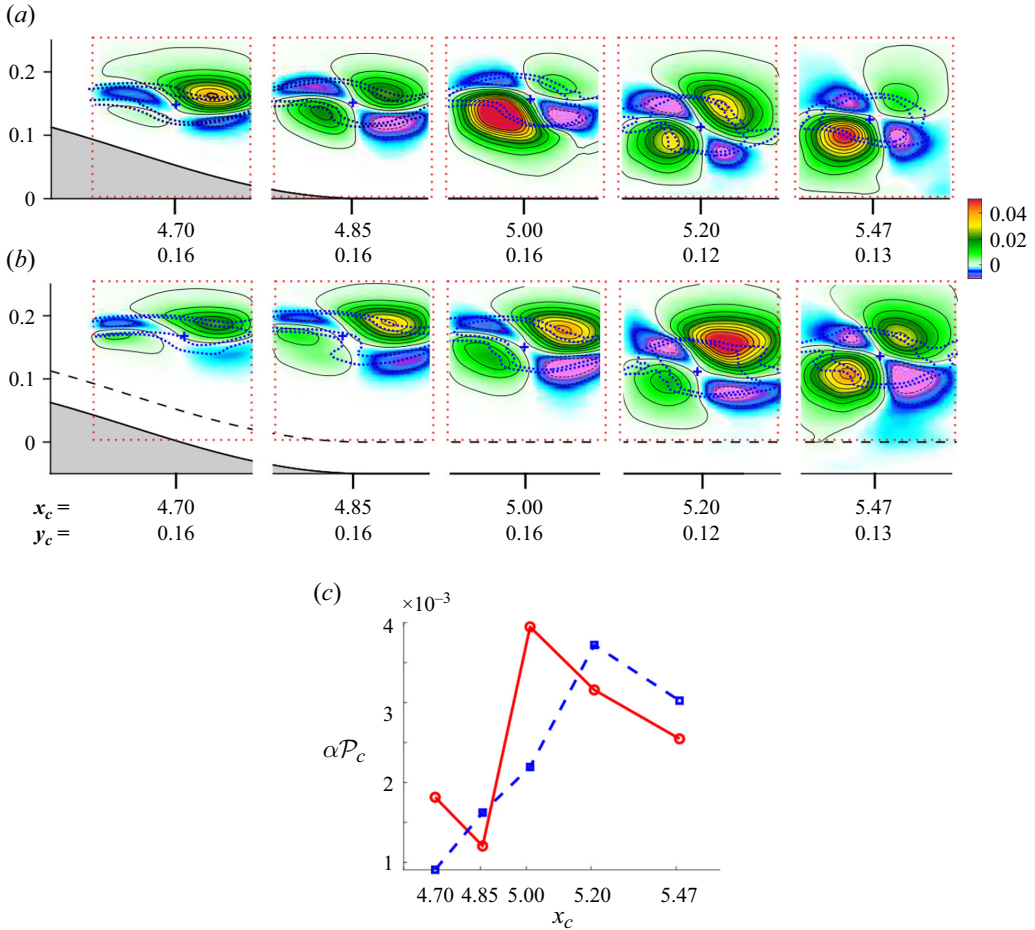


Figure 15. Coherent production, $\mathcal{P}_c = -\tilde{u}_i \tilde{u}_j \partial \langle U_i \rangle / \partial x_j$. Panel (a) is for SW, and (b) is for GW at the groove centre. Here, x_c and y_c denote the (x, y) locations of the point of alignment for education in each panel. All panels are superimposed with corresponding contours of $\tilde{\omega}_z$ at levels -1.3 and -2.3 (dotted lines). A + sign identifies the location for education alignment and is very close to the location of the $\tilde{\omega}_z$ peak. The x -range of each panel is 0.2. Panel (c) shows the \mathcal{P}_c area average over the dotted squares in (a,b), $\alpha \mathcal{P}_c = A_{square}^{-1} \iint \mathcal{P}_c dx dy$; solid line SW and dashed line GW.

and with peak values at the shear layer. Throughout all five stations, lower $[\psi''\psi'']$ is observed for GW with respect to SW (figure 16a,b). The incoherent production (production of random motion by coherent motion), $\mathcal{P}_r = -[\psi''u_j'] [S_{ij}]$, corroborates the lowered production, particularly in the core of SRs in GW, but also a reduction of the peaks in front and behind (figure 16c,d,e) – note that the peaks of \mathcal{P}_r are expected to be in front and behind of the SR where strain rate is maximum (Hussain 1983). The non-zero \mathcal{P}_r in the core of SRs emphasizes that the SRs are turbulent and not exactly uniform in z . The lower \mathcal{P}_r (particularly at the core) in GW can be attributed to the swirling jets suppressing incoherent production by organizing the flow in the form of swirling streamwise jets. The fact that there is lower \mathcal{P}_r in GW than in SW suggests that flow should be more organized (coherent); therefore, coherent measures such as $-\tilde{u}\tilde{v}$ can be expected to be higher in magnitude in GW. From figure 14(a,b), it is not evident that this is the case. The streamwise evolution trend of $-\tilde{u}\tilde{v}$ via spatial averages (figure 14c) supports this

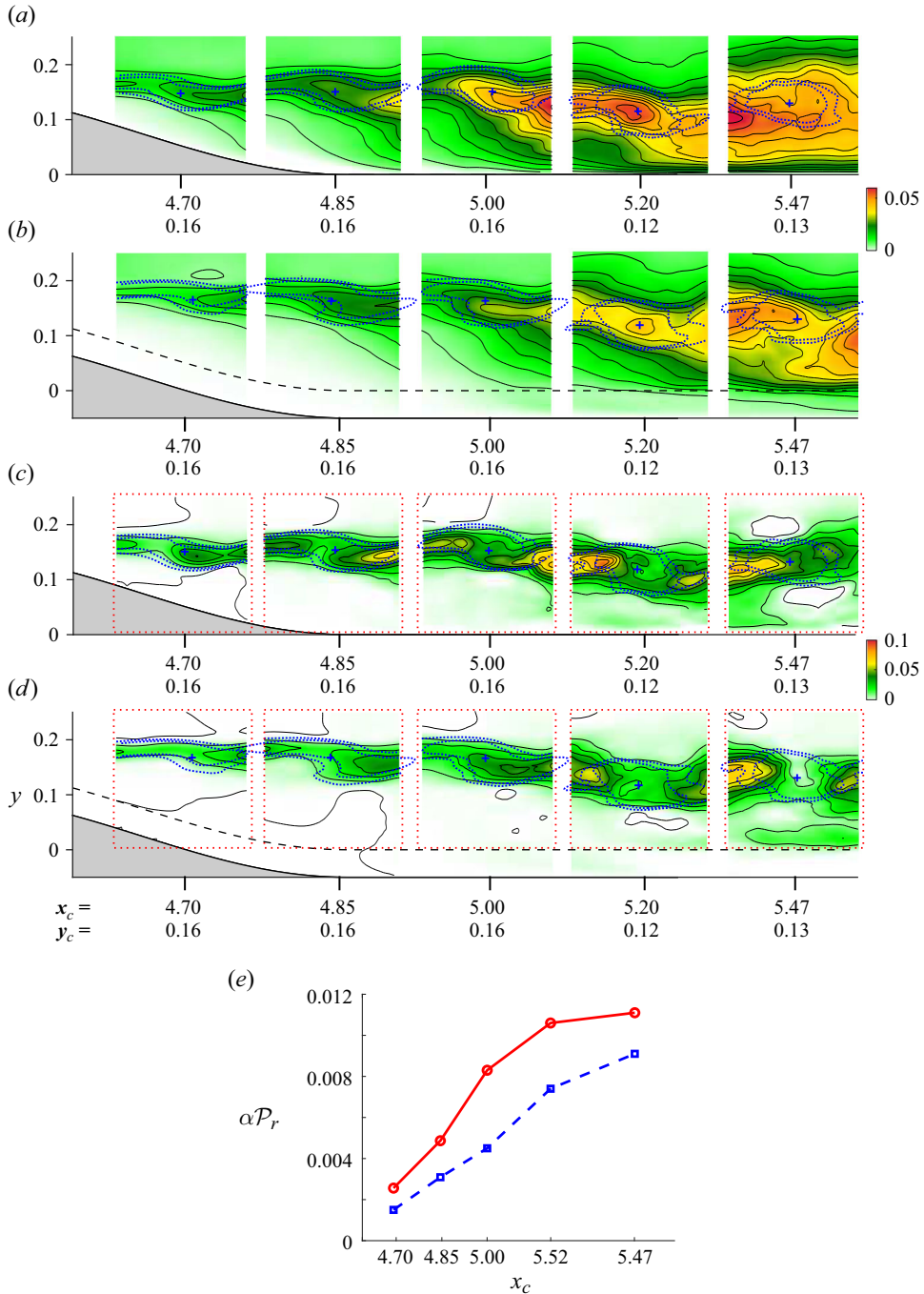


Figure 16. (a,b) Incoherent turbulence intensity, $[u''u''] + [v''v''] + [w''w'']$. (c, d) Incoherent production, $\mathcal{P}_r = -[y''u'_j][\partial U_i/\partial x_j]$. Panels (a,c) are for SW, and (b,d) for GW at the groove centre. Here, x_c and y_c denote the (x, y) locations of the point of alignment for eduction in each panel. All panels are superimposed with corresponding contours of $\tilde{\omega}_z$ at levels -1.3 and -2.3 (dotted lines). A + sign identifies the location for eduction alignment and is very close to the location of the $\tilde{\omega}_z$ peak. The x -range of each panel is 0.2. Panel (e) shows the \mathcal{P}_r area average over the dotted squares in (c,d), $\alpha \mathcal{P}_r = A_{square}^{-1} \iint \mathcal{P}_r dx dy$; solid line SW and dashed line GW.

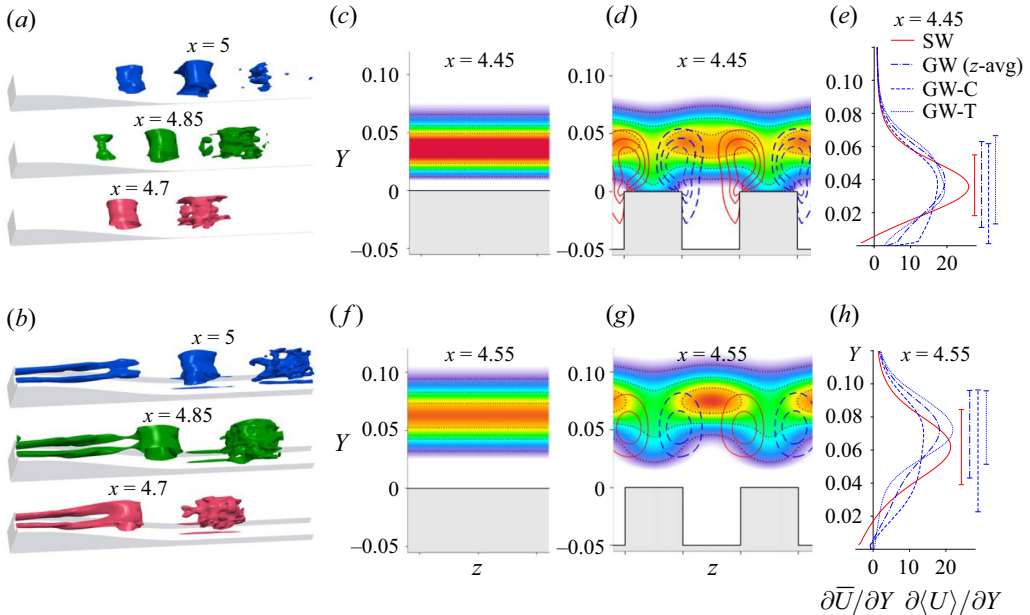


Figure 17. Three-dimensional iso-surfaces of $-\lambda_2(\partial[U_i]/\partial x_j)$ for (a) SW and (b) GW of the educed structures at different x locations (shifted in z to illustrate the time evolution). Colour maps of $\partial\bar{U}/\partial Y$ for (c,f) SW and $\partial\langle U \rangle/\partial Y$ for (d,g) GW with superimposed contours of $\langle\Omega_x\rangle$. (e) Profiles of $\partial\bar{U}/\partial Y$ for SW and $\partial\langle U \rangle/\partial Y$ for GW at the centre crests (GW-C), at the centre of grooves (GW-T) and GW spanwise averaged (GW z -avg) at different streamwise locations. The vertical bars in (e) and (h) represent the width of the profiles in these two panels; the width is measured where the value is half of the peak value of each profile.

expectation that coherent measures would be higher with lower incoherent turbulence production, particularly evident for stations at $x_c = 5.2$ and 5.47 .

The results of the coherent and incoherent measures show that SRs are more coherent in GW but generate less intense random fluctuations (turbulence intensity), seemingly by the spinning jets generated by the grooves. This confirms the inferences made from the quadrant Reynolds shear stress analysis and two-point correlations of pressure fluctuations – more coherent but weaker SRs. So far, we have focused on coherent measures in x – y planes and found evidence of the suppression of turbulence for the GW due to spinning jets but have not yet shown the spinning jets emerging from the phase average.

5.2.4. Streamwise spinning jets

It is reasonable to assume that the small streamwise spinning jets in figure 6 play an important role in modifying the SRs. In the phase-average procedure above, we only consider x – y sections where the vorticity vector is predominantly aligned with the spanwise direction ($-z$). From the two-point correlations in § 4.2, we expect an instantaneous realization of a spanwise structure at any arbitrary z location will extend at least a distance 0.1 (twice the width of a groove) in the spanwise direction, given the high correlation of all velocity components and pressure within that length scale. Thus, we examine the 3-D phase-average field within that range using the same criteria used to obtain the 2-D phase-average fields previously. Figure 17 shows iso-surfaces of λ_2 for the phase-average field at the first three stations presented in figure 13. The results for the GW case confirm the interaction of streamwise vortices attached to the corners

of grooves with the dominant SRs. As the SR starts to form, the streamwise vortices become embedded in the initial stages of the SRs (figure 17*b*). This interaction is evident at $x = 4.7$; however, at $x = 4.85$, these streamwise vortical structures become much weaker (due to cross-diffusion) and less apparent for the λ_2 threshold chosen. Note that, moving away in the z -direction from the x - y plane of the reference position, jitter is expected to increase, leading to some smearing of the deduced structure. Nevertheless, the fact that the streamwise structures attached to the SRs appear in the 3-D phase average is evidence of their coherence. The smeared SRs that emerge in front and back of the deduced SR can also be seen in the λ_2 of the phase average in figure 17(*a,b*) (also highlighted in figure 13 with yellow patches).

5.2.5. *Spanwise roller evolution in GW*

The flow induced by the grooves causes waviness of the shear layer, resembling a corrugated shear layer (Bell & Mehta 1993; Schoppa & Hussain 2002), which prevents a spanwise homogeneous inviscid (inflectional) instability (shear layer) at the onset of the shear layer. The induced wavy shear layer in GW is evident in figure 17(*d,g*) in comparison with the SW. Because of the spanwise variation introduced by the grooves and associated vortical structures, regions of high and low wall-normal velocity gradient $\partial\langle U \rangle / \partial Y$ are obtained with a certain waviness of the shear layer. The wavy shear layer overall results in a more diffuse inviscid instability (lower peak in $\partial\langle U \rangle / \partial Y$), most evident in the spanwise-averaged $\partial\langle U \rangle / \partial Y$ for GW shown in figure 17(*e,h*). The vertical bars in figure 17(*e,h*) at half of the peak of the spanwise-averaged $\partial\langle U \rangle / \partial Y$ show a 41.2% increase in thickness of the shear layer at $x = 4.45$ and 17.2% at $x = 4.55$. Although the waviness of the shear layer is a local effect in the region close to the separation point ($x = 4.4$ – 4.5), the SRs are developing from a more diffuse shear layer instability. Therefore, a different growth rate of the SRs is expected, perhaps lower for GW than SW. Certainly, this is consistent with the fact that we have a delayed peak of the turbulence in GW, i.e. the SRs are forming later, and there are changes in normal stress production $-\langle u'u' \rangle \langle S_{11} \rangle$ as documented in HYGS. At the same time, we believe that the streamwise vortices are suppressing the incoherent motion due to SRs, perhaps acting as reins preventing these from becoming more three-dimensional or delaying the transition to a more 3-D vortical structure (delaying breakup) and also suppressing the core dynamics of the SRs – hence the overall lower turbulence. This last speculation, which we cannot fully explain, contrasts with what was found in Bell & Mehta (1993), where injected streamwise vorticity into a mixing layer leads to more 3-D spanwise structures. We do agree with Bell & Mehta (1993) that perhaps the entrainment and pairing rates are being reduced due to the introduced streamwise vorticity but for different reasons here. The streamwise vortices as reins perhaps suppress the breakup of the SRs or prevent pairing, entrainment and the core dynamics. Of course, the effect of grooves in controlling SR depends on the size of the grooves, an aspect to be addressed in future investigations.

6. Separation bubble region

As discussed above, the grooves modify the SRs in their progression downstream above the separation region. However, the topic of how such modifications coupled with the underlying separation region remains unanswered. In this section, we attempt to quantify some of the key features that are related to the SB's unsteadiness.

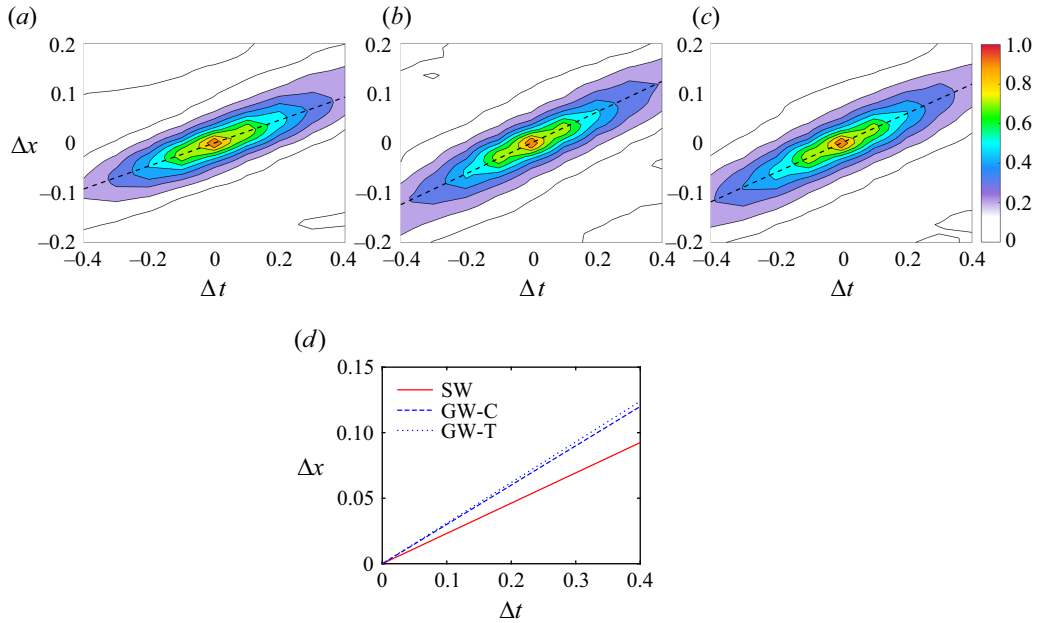


Figure 18. Space–time correlations of spanwise vorticity fluctuations $r_{\omega_z \omega_z}$ for (a) the SW, (b) the GW at the centre of grooves and (c) GW at the centre of crests; the reference point coordinates are the point of peak r.m.s. pressure fluctuations: SW at $(x_0, y_0) = (5.2, 0.12)$ and GW $(5.47, 0.134)$. (d) Line fit connecting the coordinate points with $\partial r_{\omega_z \omega_z} / \partial \Delta x = 0$ at every Δt from panels (a, b, c); solid line is SW, dashed is GW at the centre of crests (GW-C) and dotted line, GW at the centre of grooves (GW-T).

6.1. Propagation velocity of the SRs

An unanswered question is why the SB in GW is longer than that in SW. One explanation is that the fluid channelled through the grooves and ejected behind the bump pushes the SRs – resulting in a higher propagation velocity and a longer travelling distance than those in the SW case. To confirm this, the convective velocity of the SRs is investigated. Note that the computation of propagation velocity is a non-trivial task, and estimation without taking into account the size of structures can sometimes lead to errors, particularly when using Taylor’s frozen hypothesis (Zaman & Hussain 1981; Del Álamo & Jiménez 2009). Here, the propagation velocity is considered from the signal propagation velocity of instantaneous spanwise vorticity fluctuations (ω'_z) measured based on the peak locations of space–time correlations (Hussain & Clark 1981). The two-point correlation (4.3) is extended to construct space–time correlation maps by considering a time delay between the two-point variable fluctuations, defined as

$$r_{\omega_z \omega_z}(x_0, y_0, z_0, \Delta x, \Delta t) = \frac{\langle \omega'_z(x_0 + \Delta x, y_0, z_0, t + \Delta t) \omega'_z(x_0, y_0, z_0, t) \rangle}{\langle \omega'_z \omega'_z \rangle^{\frac{1}{2}}(x_0, y_0, z_0) \langle \omega'_z \omega'_z \rangle^{\frac{1}{2}}(x, y, z)}. \quad (6.1)$$

Space–time correlation contour maps of $r_{\omega_z \omega_z}$ are shown in figure 18(a–c) for SW, GW at the grooves and GW at the crests, respectively. Note that the reference points (x_0) for $r_{\omega_z \omega_z}$ (given in the caption of figure 18) are based on the location of peak pressure fluctuations – which coincide with the location of the shear layer and SRs. The propagation velocity is obtained by fitting a line connecting coordinate points with $\partial r_{\omega_z \omega_z} / \partial \Delta x = 0$ at every Δt (Hussain & Clark 1981), i.e. the local maximum correlation at every Δt . The propagation

velocities are $u_c = 0.23$ for SW, 0.31 at the centre of grooves and 0.30 at the centre of crests for GW, confirming that indeed the SRs are travelling downstream faster in GW. A lower propagation velocity at crests indicates that perhaps SRs are stretched between the crests and grooves, which would suggest waviness in the spanwise direction (see [figure 17c](#)) with a forced wavelength matching the grooves. However, the difference in propagation velocity between crests and grooves is rather small, and, as discussed before, the SRs realizations (at this x) are expected to be relatively spanwise uniform. The inferred slight waviness is just a history effect of the flow ejection at the grooves and streamwise vortices at the crest corners earlier in the shear layer.

Perhaps an additional reason for having a higher propagation velocity for the SR in GW is the image vortex and the fact that the SRs are forming from a shear layer slightly farther from the wall (compare the peaks in $\partial\langle U \rangle/\partial Y$ in [figure 17\(h\)](#) between SW and GW, from $y^+ \approx 18$ –24). The increased separation distance between the SR and image vortex within the wall would reduce the upstream induced velocity (SRs have naturally $-\omega'_z$, and the induced motion with their image would be in the $-x$ direction), hence increasing the SR downstream velocity.

6.2. Unsteadiness of the separation bubble

We use the point of zero wall shear stress ($\tau_w = 0$) to identify the point of reattachment for both SW and GW – this criterion for GW was shown by HGYS to be in agreement with various other criteria. The instantaneous detachment/reattachment lines are approximately uniform in the spanwise direction ([figure 19a,b](#)); the uniform detachment/reattachment lines have also been observed for the backward-facing step (Le, Moin & Kim 1997) and flow separation due to APG (Na & Moin 1998; Wu & Piomelli 2018). Therefore, as in Le *et al.* (1997) and Na & Moin (1998), we track the location of the reattachment point (x_r) based on the spanwise-averaged wall shear stress ($\tau_{w,zavg}$) (for the GW case, spanwise averaging is performed at the same relative positions of the grooves). Specifically, the reattachment point is defined where $\tau_{w,zavg}$ switches from negative to positive ([figure 19c–e](#)).

The instantaneous detachment/reattachment lines and overall SB motions, not surprisingly, are linked with the SRs that develop in the shear layer after flow separation (rollup frequency) and shedding of vorticity of the SB (Eaton & Johnston 1980; Neto *et al.* 1993). Since the grooves change the SRs, we further investigate how the GW modifies the unsteadiness of the x_r .

[Figure 20](#) shows histograms of the downstream travelled distance Δ_{x_r} and time rate of increase of the streamwise travel distance m_{x_r} ; the latter illustrating the speed of x_r . The travelled distances (Δ_{x_r}) are obtained by starting at the instant when the reattachment position changes direction from moving upstream to downstream and ending at the opposite situation, i.e. from a local minimum to a local maximum in [figure 19\(c–e\)](#). The Δ_{x_r} probability distribution for GW shows many occurrences for larger lengths of the SB compared with SW, particularly at the centre of grooves. Such increased probability of large Δ_{x_r} suggests that the grooves somewhat stabilize the growth of the SB, allowing for longer travelled distances of x_r and modifying the shedding dynamics of the SB.

The histogram of m_{x_r} establishes that the travelling speed of x_r for the GW is higher than the SW case, with a more noticeable increase at troughs ([figure 20b](#)). More importantly, the mean values of m_{x_r} coincide with the propagation velocity obtained based on r_{ω_z, ω_z} at the shear layer in § 6.1. Therefore, the histogram of the slopes confirms that the movement of the SRs at the shear layer indeed leads the movement of the reattachment point, which

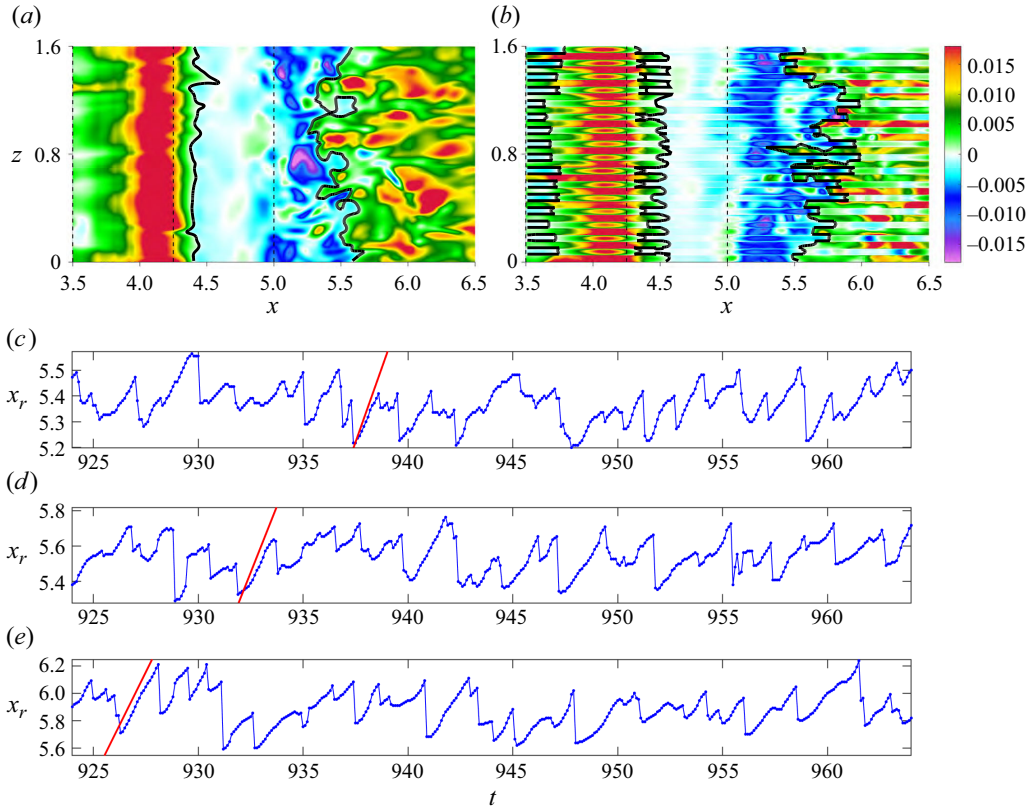


Figure 19. Instantaneous colour maps of wall shear stress, τ_w , for (a) SW and (b) GW. The thick black solid line denotes the location with $\tau_w = 0$ continuously connected through the span of the wall. Locations of spanwise-averaged reattachment point x_r for (c) SW, (d) GW at the centre of crests and (e) GW at the centre of grooves. In (c–e), the red solid line has a slope equal to the convective velocity obtained in the previous section for each configuration, respectively, as a reference.

travels at a higher speed for the GW case. Note that more occurrences with low m_{x_r} are observed at crests, which agrees with the slightly slower propagation velocity at crests.

The sudden retraction of x_r is due to the shedding of vorticity from the SB, which clearly shows a quasi-periodic behaviour in the signal shown in figure 19(c–e). This periodic behaviour is not necessarily connected with the rollup frequency of SRs – as we will see later – but with the saturation of the growth of the SB and the drag that it is subjected to, having a characteristic shedding frequency.

The unsteadiness of the reattachment point can be quantified based on the standard deviation of x_r (0.071 for the SW and 0.131 and 0.101 at the grooves and crests for GW, respectively), notably increasing for the GW. The higher standard deviation of x_r in GW is attributed to the more prevalent minibubbles that can reach further downstream, as figure 13(f–j) shows, which is expected to alter the shedding of vorticity from the SB.

The rollup frequency of SRs, quantified by the spectra of the signal

$$\Gamma(t) = \int_{0.11}^{0.21} \Omega_{z,zavg}(x = 4.9, y, t) dy, \quad (6.2)$$

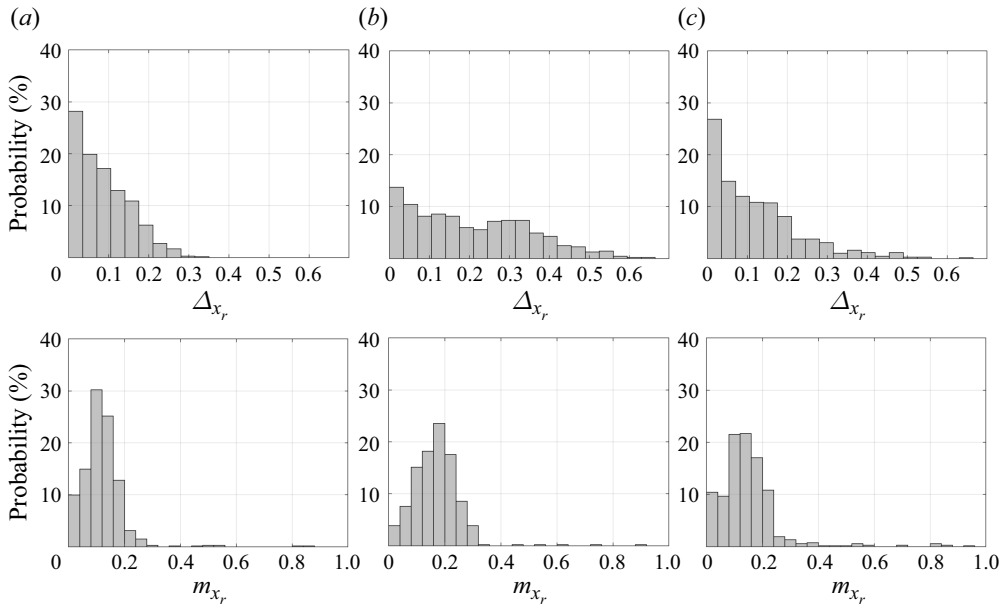


Figure 20. Histogram of downstream travelled length (Δx_r) and the slope (m_{x_r}) of the rate of increase in the downstream travelled length from the time series of x_r for (a) SW, (b) GW at the centre of grooves and (c) GW at the centre of crests.

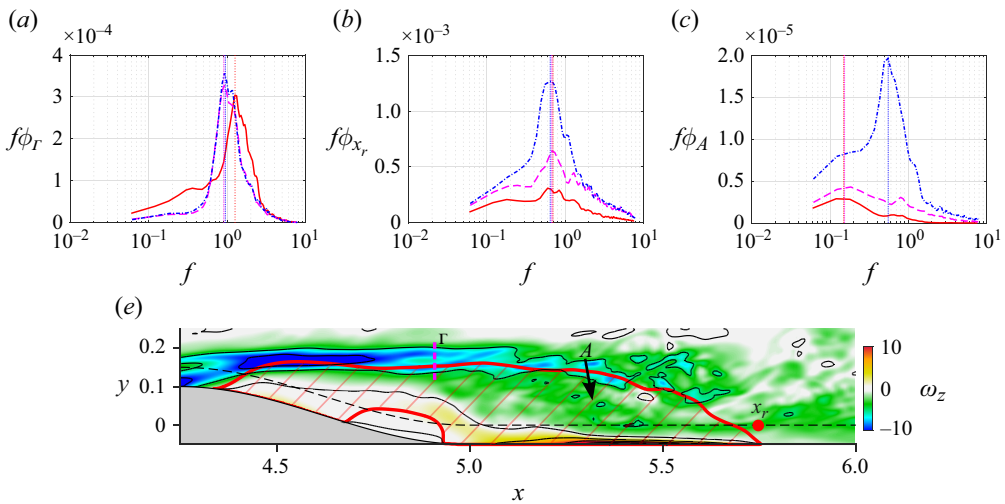


Figure 21. Pre-multiplied frequency spectra of (a) spanwise vorticity vertically integrated across the shear layer at $x = 4.9$, Γ , (b) the reattachment position x_r and (c) the SB area (A). The solid line is SW, the dashed line is GW at the centre of crests (GW-C) and the dash-dot line is GW at the centre of grooves (GW-T). (d) An instantaneous snapshot as reference for the computations of Γ , A and x_r , as suggested by a referee.

(figure 21a; the shear layer is located between $y = 0.11$ and 0.21 , as seen in figure 13) shows that the peak frequency in GW is lower than SW, consistent with pressure correlations in § 4.2. Perhaps this behaviour is expected since the shear layer in GW is more diffused in y and with a lower peak in $\partial\langle U \rangle / \partial y$, so the rollup process takes longer.

On the other hand, the peak frequency in the spectra of x_r is found to be lower – for both SW and GW – than the rollup of SRs (figure 21*b*). As mentioned before, the peak frequencies of x_r are found to characterize the shedding of vorticity from the SB, verified via a movie visualization (available as supplementary material at <https://doi.org/10.1017/jfm.2025.4>) of the SB synchronized with the evolution of the reattachment position. Interestingly, the grooves do not affect the peak frequency of x_r with respect to SW. However, the magnitude of ϕ_{x_r} for the peak frequency is significantly different between GW and SW, and different from that observed for ϕ_Γ . This means that, while the peak frequency of x_r remains the same between SW and GW, in GW, the amplitude of the oscillations is larger, as previously pointed out through the histogram of Δx_r in figure 20(*a–c*). Perhaps the grooves are facilitating the movement of the reattachment point by inducing an effective slip velocity at the wall.

We also examine the spectra of the SB area, A (computed similarly to that in Fang *et al.* (2021)), as follows:

$$A(t) = \int_0^H \int_{4.25}^{12} I_A(\psi) dx dy; \quad I_A(\psi) = \begin{cases} 1, & \psi < 0, \\ 0, & \text{otherwise,} \end{cases} \quad (6.3)$$

$$\psi(x, y, t) = \int_{y=wall}^y U(x, y')_{z-avg} dy',$$

and as shown in figure 21(*c*) (integrated from $x = 4.25$ where the peak of the bump is to the end of the channel at $x = 12$). Unlike Γ or x_r , which are localized measurements, A provides information about the instantaneous size of the SB by integrating large-scale and small-scale phenomena. The A spectrum for SW exhibits a distinct peak at a low frequency $f = 0.12$. Several researchers have reported such low-frequency oscillations (Hudy & Naguib 2007; Wu *et al.* 2020; Fang *et al.* 2021), which are frequently referred to as the ‘breathing’ motions of the SB; however, no consensus has been reached regarding their origin. This low-frequency peak also agrees with the results obtained by Eaton & Johnston (1980); Hudy & Naguib (2007) for a backward-facing step separating flow. The A spectra in SW also show a higher peak frequency – perhaps not so clear as the magnitude of ϕ_A is very low – which is very close to the shedding frequency of vorticity from the SB as quantified through ϕ_{x_r} . The rollup frequency, as quantified through ϕ_Γ , does not clearly surface in the spectra of A . This is not surprising since the rollup process only distorts the upper surface of the SB, changing the area minimally (see movie in the supplementary material).

In GW, at the centre of the grooves, the peak frequency of the A is the shedding frequency of the SB, which completely dominates over the low-frequency peak; while at crests, the low frequency is dominant, and the shedding frequency peak becomes more noticeable. In addition, like ϕ_{x_r} , the corresponding peak magnitude in GW at the centre of grooves significantly increases.

7. Average ‘negative production’

We delineate and discuss here the different sources of negative (turbulent kinetic energy, TKE) production for a representative figure, figure 22, reproduced from HGYS (their figure 19).

The average production in SW is

$$\overline{\mathcal{P}} = \underbrace{-\overline{uu}S_{11}}_{\overline{\mathcal{P}}_{uu}} - \underbrace{\overline{vv}S_{22}}_{\overline{\mathcal{P}}_{vv}} - \underbrace{2\overline{uv}S_{12}}_{\overline{\mathcal{P}}_{uv}}. \quad (7.1)$$

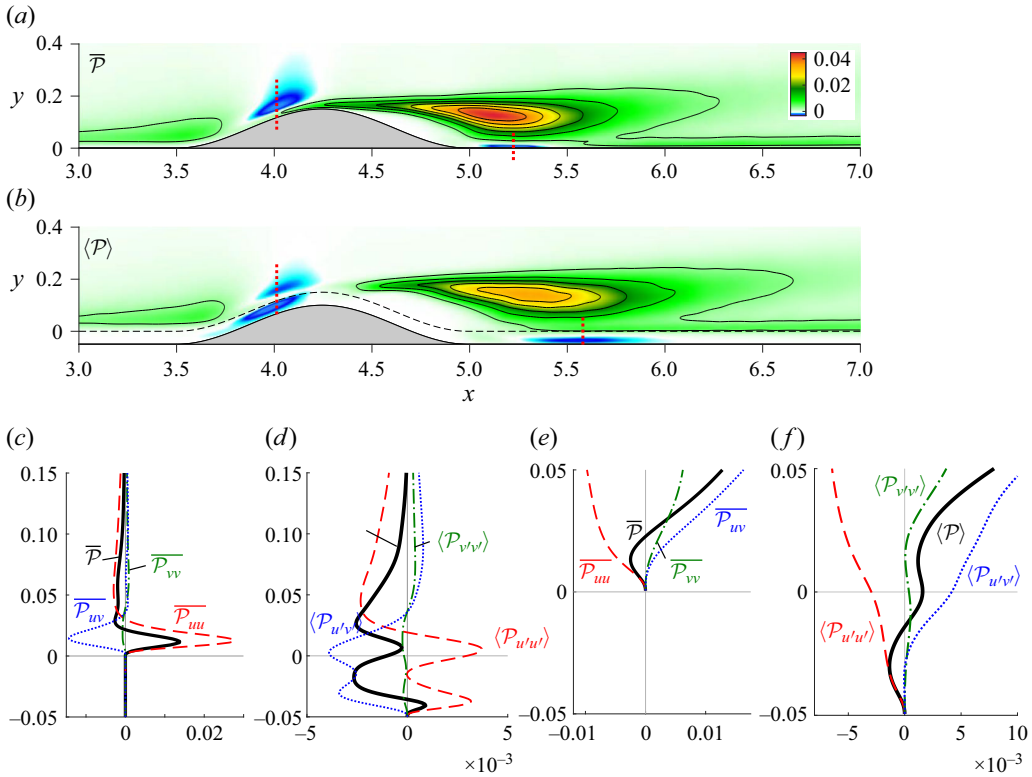


Figure 22. Colour maps of turbulent kinetic energy (TKE) production for (a) SW and (b) GW at the centre of grooves. Wall-normal profiles of production and the separate contributions from Reynolds normal stresses and Reynolds shear stress at (c,d) $x = 4.05$ where flow accelerates and at (e,f) $x = 5.625$ inside the SB; (c,e) SW and (d,f) GW.

In GW, the average production is

$$\langle \mathcal{P} \rangle \approx \underbrace{-\langle u'u' \rangle \langle S_{11} \rangle}_{\langle \mathcal{P}_{u'u'} \rangle} - \underbrace{\langle v'v' \rangle \langle S_{22} \rangle}_{\langle \mathcal{P}_{v'v'} \rangle} - 2 \underbrace{\langle u'v' \rangle \langle S_{12} \rangle}_{\langle \mathcal{P}_{u'v'} \rangle}; \quad (7.2)$$

and the contributions from $-\langle w'w' \rangle \langle S_{33} \rangle$, $-2\langle u'w' \rangle \langle S_{13} \rangle$ and $-2\langle v'w' \rangle \langle S_{23} \rangle$ are negligible in the regions of $-\langle \mathcal{P} \rangle$. In SW, $-\overline{\mathcal{P}}$ is found in the upstream side of the bump and in the near-wall flow inside the SB (figure 22a); in GW, an additional region of negative $\langle \mathcal{P} \rangle$ is found inside the grooves in the upstream side of the bump (figure 22b). On the upstream side of the (SW) bump, the origin of negative $\overline{\mathcal{P}}$ is due to the mean stretching of fluid elements, i.e. the term $\overline{\mathcal{P}_{uu}}$ (streamwise normal production) being negative dominating over the other terms in $\overline{\mathcal{P}}$ (figure 22c); in GW, above the crests (i.e. $Y > 0$) the value of $-\langle \mathcal{P} \rangle$ is similarly due to $-\langle \mathcal{P}_{u'u'} \rangle$ (figure 22d). Inside the grooves, the negative $\langle \mathcal{P} \rangle$ is due to counter-gradient Reynolds shear stress (either Q1 events with $u' > 0$ and $v' > 0$ or Q3 events with $u' < 0$ and $v' < 0$) leading to $-\langle \mathcal{P}_{u'v'} \rangle$ (net negative time-averaged shear production) dominating over the other terms in $\langle \mathcal{P} \rangle$ (figure 22d). The negative production inside the SB near the wall for both SW and GW is due to the mean streamwise stretching of fluid elements, $-\overline{\mathcal{P}_{uu}}$ in SW and $-\langle \mathcal{P}_{u'u'} \rangle$ in GW (figure 22e-f).

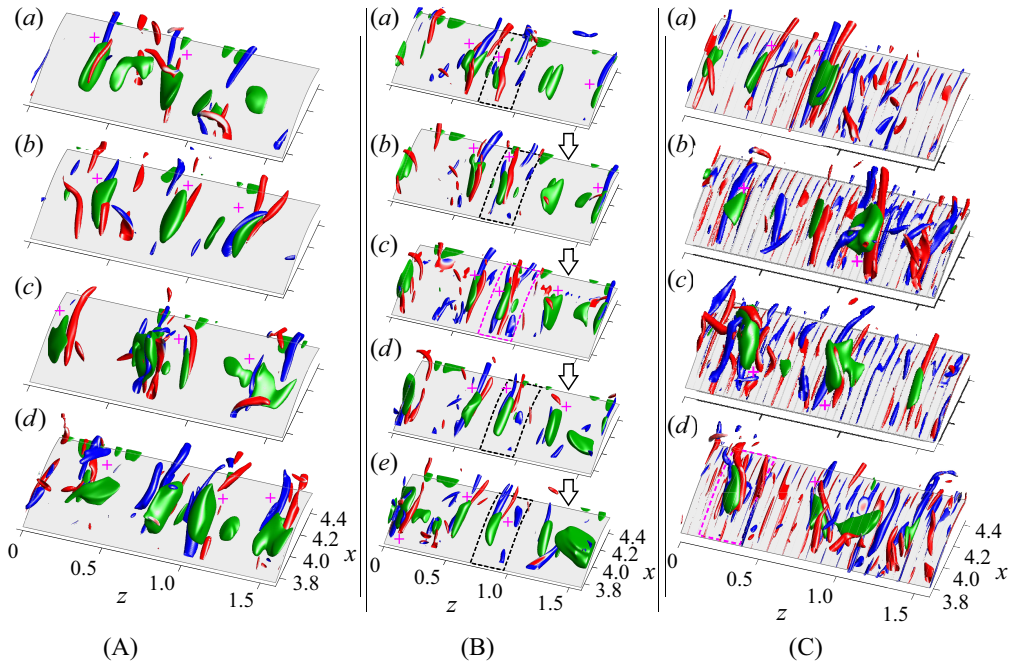


Figure 23. Iso-surfaces of $-\lambda_2$ coloured by ω'_x (red $+\omega'_x$ and blue $-\omega'_x$) and negative production due to normal Reynolds stress ($-\mathcal{P}_{uu}$, $-\mathcal{P}_{u'u'}$) in green. (A) Random snapshots SW; (B) sequence snapshots SW; (C) random snapshots GW.

Here, we want to discuss further the mechanism of $-\overline{\mathcal{P}}$ in SW and $-\langle \mathcal{P} \rangle$ in GW in terms of the instantaneous flow structures, with emphasis on the upstream side of the bump where flow accelerates. For this, we searched for regions of instantaneous negative production due to streamwise stretching, $\mathcal{P}_{uu} (\equiv -uu\overline{S_{11}}) < 0$ in SW and counter-gradient Reynolds shear stress $\mathcal{P}_{u'v'} (\equiv -u'v'\langle S_{11} \rangle) < 0$ in GW, along with visualization of λ_2 structures (figure 23). Regions of $-\mathcal{P}_{uu}$ are often found in between two streamwise vortices of opposite sign vorticity ω_x (vortex dipole) where the left one has $-\omega_x$ – these regions are identified with a plus sign in figure 23A – although, there are some instances of $-\mathcal{P}_{uu}$ occurring by a single streamwise-aligned $-\lambda_2$ structure. Cases of $-\mathcal{P}_{uu}$ without $-\lambda_2$ structures are due to similar situations, but a lower threshold in λ_2 is needed. In the time sequence of figure 23B, we see that the regions of $-\mathcal{P}_{uu}$ (green patches) remain approximately of the same size as the streamwise vortices travel downstream through the region of $+\overline{S_{11}}$. Also, we see that, even when the streamwise vortices have almost left the region of $+\overline{S_{11}}$, the tails are strong enough to keep inducing regions of $-\mathcal{P}_{uu}$. In GW, we find similar events of generation of $-\mathcal{P}_{u'u'}$ between the two counter-rotating vortices (figure 23C. Of course, because of the grooves, the $-\lambda_2$ structures appear slightly more chaotic with many smaller-scale structures. Distinctive to GW is the $-\lambda_2$ at the corner of crests, as on the upstream side of the bump, the flow enters the grooves, gets channelled and ejects around the peak of the bump, leading to the rollup of vorticity in these regions.

Additional details are discussed by zooming in on the event of $-\mathcal{P}_{uu}$ marked by the magenta dashed box in figure 23B(c) and shown in figure 24(a). The vortex dipole induces $+v$ (figure 24c), which is accompanied by $-u$ (figure 24b), a co-gradient Reynolds shear stress Q2 event. Even though we have positive shear stress production ($+\mathcal{P}_{uv}$) actually there is a net $-\mathcal{P}$ for this Q2 (co-gradient stress) event (figure 24b,c). Inspection of all

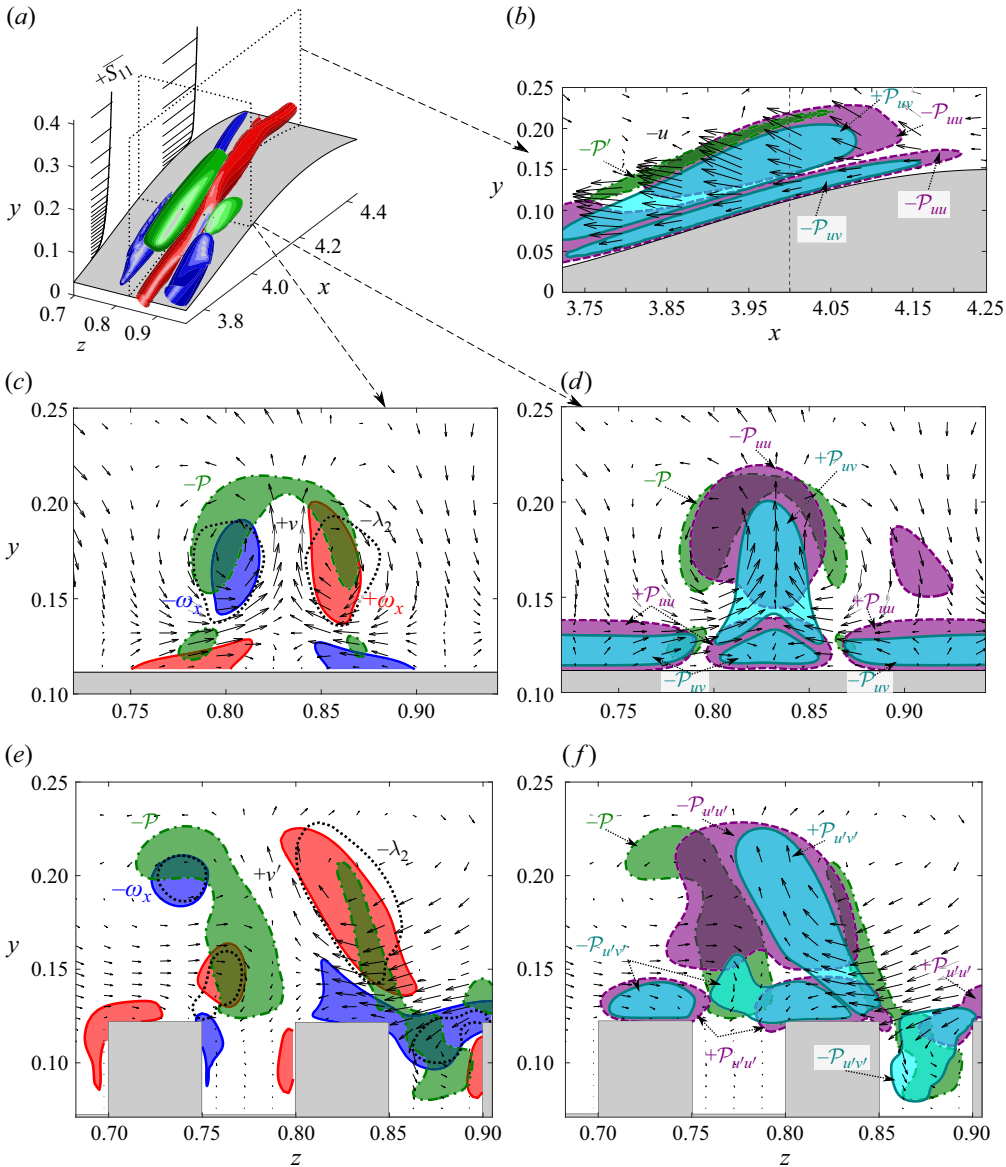


Figure 24. (a) Zoomed-in view of figure 23B(c) with xy plane shown in (b) and yz plane shown in (c) and (d). A similar subregion is taken from figure 23C(d) and shown in a yz plane in (e) and (f). Panels (c) and (e) show ω_x (positive in red, negative in blue) and $-\lambda_2$ (black). Here, $-\mathcal{P}$ is shown in green in all panels. Panels (b), (d) and (f) show \mathcal{P}_{uu} (or $\mathcal{P}'_{u'u'}$) as purple and \mathcal{P}_{uv} (or $\mathcal{P}'_{u'v'}$) in light blue.

the contributions to production (figure 24d) shows that the $-\mathcal{P}$ originates from $-\mathcal{P}_{uu}$, i.e. $+\overline{S}_{11}$ streamwise stretching of fluid elements in this accelerating flow region leading to $-\mathcal{P}_{uu}$, as already indicated by the mean production in HGYS. Note that part of the region with $-\mathcal{P}_{uu}$ (approximately with a circle shape) is countered by $+\mathcal{P}_{uv}$, so that the net $-\mathcal{P}$ has a hat or crescent shape. There are several regions of $-\mathcal{P}_{uv}$ near the wall, although no mean negative production due to a counter-gradient is found in SW (HGYS). The $-\mathcal{P}_{uv}$ regions are cancelled by regions of greater magnitude of $+\mathcal{P}_{uu}$ (figure 24b,d). The fluid elements near the wall experience compression (i.e. $-\overline{S}_{11}$), consistent with the

near-wall APG induced by mean streamline curvature discussed in detail in HGYS – hence obtaining $+\mathcal{P}_{uu}$.

Zoomed-in yz cross-sections are also performed for GW in the dashed box of figure 23(c,d) and shown in figure 24(e,f). Similar to SW, vortex pairs are found inducing $-\mathcal{P}$ on a Q2 event (figure 24e) – although not as organized as that chosen in SW. The generation of $-\mathcal{P}$ above the crests is similar to that in SW due to $-\mathcal{P}_{u'u'}$ – the streamwise stretching of fluid elements. Here, it is shown that the $-\mathcal{P}$ that occurs inside grooves – shown in HGYS to be on average due to the counter-gradient Reynolds stress – is connected with a vortical structure penetrating into the grooves. In this case, the vortex structure has $-\omega_x$ inducing a Q3 event inside the groove (figure 24e). In agreement with HGYS, the $-\mathcal{P}$ inside grooves is due to $-\mathcal{P}_{u'v'}$, i.e. counter-gradient Reynolds shear stress (figure 24f). Likely, similar results will result from a vortex with $+\omega'_x$ that penetrates into the grooves. As mentioned already, in SW this situation occurs where the pair of vortices with different signs of vorticity induce regions of $-\mathcal{P}_{uv}$ near the wall but there countered by $+\mathcal{P}_{uu}$; in GW the grooves suppress the compression of fluid elements as the fluid is channelled, allowing for the counter-gradient negative mean production.

The brief analysis indicates two common features for negative production – streamwise stretching of dipoles in FPGs and channelling of vortical structures into the grooves – opening up possible avenues of future CS research to further understand the possible applications of this dynamics to flow control.

8. Concluding discussion

Following the work by HGYS, the dynamics of CSs for a separated TBL due to a transverse bump superimposed with longitudinal grooves is detailed. This flow features several interesting phenomena: incipient separation and (average) negative production in the accelerating flow upstream of the bump, as well as a SB downstream of the bump, including near-wall SBs of reverse circulation (minibubbles), etc. In GW, the flow enters the grooves on the upstream side of the bump and ejects downstream near the bump peak. This ejection causes the flow to rotate at each crest corner, generating a spanwise series of alternatively counter-swirling streamwise jets that merge with the shear layer from the peak of the bump, altering the rollup of SRs.

8.1. Coherent structure dynamics and its quadrant analysis

The quadrant analysis demonstrates that the time-averaged Reynolds shear stress, which results from strong sweep (Q4) and ejections (Q2) (associated with the SRs), decreases in GW. From the CS analysis, SR generates sweep downstream of the structure and ejection upstream for both SW and GW. The grooves generate a series of streamwise jets with ejections and sweeps, the former stronger than the latter, in $y-z$ planes, which interact and modify the SR ejections and sweeps. The quadrant analysis shows that the swirling jet ejections are effective in countering the SR sweeps, weakening the Q4 Reynolds shear stress. This effect is more prominent at the initiation of the shear layer close to the bump peak because the swirling jets impact there first. The peaks in Reynolds shear stress from strong events (sweeps and ejections) for GW shift in y farther from the wall, induced by the jetting effect at the groove centres.

8.2. Coherent structure characterization via two-point correlations

Two-point velocity correlations, as expected, also identify SRs behind the bump peak, particularly that from wall-normal velocity, for both SW and GW. The grooves have a

significant effect on the streamwise velocity correlations, which decrease faster in x than in SW. Moreover, this decrease suggests that near-wall vortex rods at steep angles are more prevalent in GW. Interestingly, while the two-point correlations of pressure highlight the SRs, the correlation extends more in the z -direction for GW than SW, suggesting that grooves increase z coherence. Since the spanwise row of streamwise swirling jets all start at the same x and have virtually the same circulation, their evolution will be identical, and hence their interaction at the point of their maturity makes SRs aligned in z . Also, the streamwise correlation of pressure fluctuations in the shear layer reveals that SRs are farther apart on average in GW, suggesting a lower frequency of rollup of SRs.

8.3. Minibubbles, their role in form and skin-friction drag

Analysis via phase-average eduction of SRs reveals several new features. Surprisingly, the minibubble is persistently present in the coherent velocity field, suggesting a direct link between SRs and minibubbles – for both SW and GW. Although the importance of minibubbles is not well established, its omnipresence tells us that it is fundamental to perhaps most separated flows and likely will help us to understand flow phenomena (e.g. mass transport) over mountains, dunes, etc. In the case of GW, the minibubbles are more numerous, larger and stronger (higher circulation) compared with SW, each of which has a notable effect on both skin-friction and form drag.

8.4. Spanwise rollers and their persistent contribution to positive production

The rollup of a plane shear layer, whether initially laminar or turbulent, starts with the formation of an elliptic cross-sectioned SR tilted downward on its downstream side, transitions into a circular cross-section and then tilts its downstream side upward – as in a tumbling manner. The locations of these orientations are random as the SR advects downstream, with the time average reflecting no clear footprint of any particular SR geometry, and hence, production is always positive. In the case of the shear layer enveloping the SB, the upstream inclination of the initial elliptical SR is repeated and sustained in space (with minimized tumbling). As a consequence, the production is always positive, even instantaneously, leading to a higher positive production than in a typical plane shear layer. That is, the SRs always generate a higher time-averaged coherent Reynolds shear stress compared with a plane shear layer, where the time-averaged coherent Reynolds shear stress is much lower.

8.5. Coherent and incoherent productions

Coherent production, \mathcal{P}_c , of SRs becomes maximum upstream of the peak total turbulence production for both SW and GW. The subsequent decay in \mathcal{P}_c is expected as the mean shear decreases faster than the increase of $-\tilde{u}\tilde{v}$. These results naturally imply that the control of the SRs in the shear layer needs to occur upstream of the peak of turbulence in the uncontrolled scenario.

The incoherent production \mathcal{P}_r indeed shows its peak value at the same location as the total turbulence production. The value of \mathcal{P}_r is lower in GW than in SW by an average of 25 % (figure 16c,d) due to the reduced $\partial\langle U\rangle/\partial y$ across the shear layer. The shear layer commences as wavy as well as thicker in GW compared with SW, and the streamwise jets accentuate the waviness, with the net effect that, in GW, $\partial\langle U\rangle/\partial y$ is smaller (concomitantly SRs are larger); hence, the reduced incoherent production and turbulence intensity. Based on the educed 3-D structure, we speculate that the streamwise structures induced by the grooves prevent breakup, pairing and the core dynamics of the SRs.

8.6. Spanwise roller rollup, their propagation velocity and SB reattachment

In HGYS, we found that the SB is longer (approximately 20%) in GW than SW and attributed this to the jetting induced by the grooves. Here, we articulated that it is the jetting of fluid from grooves at the bump peak that pushes the SRs, inducing a higher propagation velocity of the SRs, hence their longer travel before impingement on the wall for reattachment. Space–time correlation maps of spanwise vorticity fluctuations verify that SRs have higher propagation velocity (20 %) in GW.

8.7. Time-dependent dynamics of SB

We identify two main flow features of SB unsteadiness: high-frequency vorticity shedding from the SB and low-frequency ‘breathing’ of SB. In SW, the low-frequency area fluctuations are stronger, while in GW, the high-frequency fluctuations are stronger. The spanwise organization by the swirling jets does not seem to be quite in consonance with this behaviour of the SB, and this begs a rigorous study of the SB dynamics with and without grooves.

8.8. Negative production

Inspection of instantaneous vortical structures using the λ_2 -criterion, along with instantaneous regions of negative production, elucidated the vortex organization that leads to the average negative production reported in HGYS. The average negative production obtained on the upstream side of the bump where flow accelerates due to streamwise stretching of fluid elements occurs every time two counter-rotating vortices appear in the accelerating region, inducing a strong ejection (Q2) event. This is somewhat counter-intuitive as this is the typical situation in flat wall turbulence, but if it occurs in a region of $+\partial\langle U\rangle/\partial x$, it leads to a significant transfer of energy from the turbulent field to the mean field. In GW, the additional region of negative production due to counter-gradient Reynolds shear stress is due to vortical structures entering the grooves, possibly connecting groove size and CS diameter as a way to modify negative production around the bump.

Supplementary material. Supplementary material is available at <https://doi.org/10.1017/jfm.2025.4>.

Acknowledgements. The authors deeply appreciate a careful review of the manuscript by N. Malik. Computational resources provided by Texas Tech University HPCC are acknowledged.

Declaration of interests. The authors report no conflict of interest.

REFERENCES

- ADRIAN, R. J. & MARUSIC, I. 2012 Coherent structures in flow over hydraulic engineering surfaces. *J. Hydraul. Res.* **50** (5), 451–464.
- ANTONIA, R. 1981 Conditional sampling in turbulence measurement. *Annu. Rev. Fluid Mech.* **13** (1), 131–156.
- BANCHETTI, J., LUCHINI, P. & QUADRIO, M. 2020 Turbulent drag reduction over curved walls. *J. Fluid Mech.* **896**, A10.
- BELL, J. H. & MEHTA, R. D. 1993 Effects of imposed spanwise perturbations on plane mixing-layer structure. *J. Fluid Mech.* **257** (1), 33–63.
- BERKOOZ, G., HOLMES, P. & LUMLEY, J. 1993 The proper orthogonal, decomposition in the analysis of turbulent flows. *Annu. Rev. Fluid Mech.* **25** (1), 539–575.
- CASTRO, I. P., KIM, J., STROH, A. & LIM, H. 2021 Channel flow with large longitudinal ribs. *J. Fluid Mech.* **915**, 1–28.
- CHOI, H., MOIN, P. & KIM, J. 1994 Active turbulence control for drag reduction in wall-bounded flows. *J. Fluid Mech.* **262** (A), 75–110.
- CIMARELLI, A., LEONFORTE, A., DE ANGELIS, E., CRIVELLINI, A. & ANGELI, D. 2019 On negative turbulence production phenomena in the shear layer of separating and reattaching flows. *Phys. Lett. A* **383** (10), 1019–1026.

- DUONG, A. H., CORKE, T. C. & THOMAS, F. O. 2021 Characteristics of drag-reduced turbulent boundary layers with pulsed-direct-current plasma actuation. *J. Fluid Mech.* **915**, A113.
- EATON, J. & JOHNSTON, J. 1980 Turbulent flow reattachment: an experimental study of the flow and structure behind a backward-facing step. *Report*. Stanford University.
- ELYASI, M. & GHAEMI, S. 2019 Experimental investigation of coherent structures of a three-dimensional separated turbulent boundary layer. *J. Fluid Mech.* **859**, 1–32.
- ENDRIKAT, S., MODESTI, D., GARCÍA-MAYORAL, R., HUTCHINS, N. & CHUNG, D. 2021 Influence of riblet shapes on the occurrence of Kelvin–Helmholtz rollers. *J. Fluid Mech.* **913**, A37.
- FANG, X., TACHIE, M. F., BERGSTROM, D. J., YANG, Z. & WANG, B.-C. 2021 Three-dimensional structural characteristics of flow separation induced by a forward-facing step in a turbulent channel flow. *J. Fluid Mech.* **919**, 1–32.
- GARCÍA-MAYORAL, R. & JIMÉNEZ, J. 2011 Hydrodynamic stability and breakdown of the viscous regime over riblets. *J. Fluid Mech.* **678**, 317–347.
- GATTI, D. & QUADRIO, M. 2016 Reynolds-number dependence of turbulent skin-friction drag reduction induced by spanwise forcing. *J. Fluid Mech.* **802**, 553–582.
- GENCE, J. & MATHIEU, J. 1979 On the application of successive plane strains to grid-generated turbulence. *J. Fluid Mech.* **93** (3), 501–513.
- GOLDSTEIN, D. & TUAN, T. 1998 Secondary flow induced by riblets. *J. Fluid Mech.* **363**, 115–151.
- HAMILTON, J., KIM, J. & WALEFFE, F. 1995 Regeneration mechanisms of near-wall turbulence structures. *J. Fluid Mech.* **25**, 317–348.
- HICKEY, J.-P., HUSSAIN, F. & WU, X. 2013 Role of coherent structures in multiple self-similar states of turbulent planar wakes. *J. Fluid Mech.* **731**, 312–363.
- HUDY, L. M. & NAGUIB, A. 2007 Stochastic estimation of a separated-flow field using wall-pressure-array measurements. *Phys. Fluids* **19** (2), 024103.
- HUSSAIN, A. & CLARK, A. 1981 Measurements of wavenumber-celerity spectrum in plane and axisymmetric jets. *AIAA J.* **19** (1), 51–55.
- HUSSAIN, A. & REYNOLDS, W. 1970 The mechanics of an organized wave in turbulent shear flow. *J. Fluid Mech.* **41** (2), 241–258.
- HUSSAIN, A. & ZAMAN, K. 1980 Vortex pairing in a circular jet under controlled excitation. Part 2. Coherent structure dynamics. *J. Fluid Mech.* **101** (3), 493–544.
- HUSSAIN, F., GARCÍA, E., YAO, J. & STOUT, E. 2024 Wall turbulence perturbed by a bump with organized small-scale roughness: flow statistics. *J. Fluid Mech.* **989**, A13.
- HUSSAIN, F. 1983 Coherent structures – reality and myth. *Phys. Fluids* **26** (10), 2816–2850.
- HUSSAIN, F. 1986 Coherent structures and turbulence. *J. Fluid Mech.* **173**, 303–356.
- HUSSAIN, F. & HAYAKAWA, M. 1987 Eduction of large-scale organized structures in a turbulent plane wake. *J. Fluid Mech.* **180** (1), 193–229.
- HUSSAIN, M. & HASAN, Z. 1985 Turbulence suppression in free turbulent shear flows under controlled excitation. Part 2. Jet-noise reduction. *J. Fluid Mech.* **150**, 159–168.
- HWANG, H. G. & LEE, J. H. 2018 Secondary flows in turbulent boundary layers over longitudinal surface roughness. *Phys. Rev. Fluid* **3** (1), 1–25.
- JEONG, J. & HUSSAIN, F. 1995 On the identification of a vortex. *J. Fluid Mech.* **285**, 69–94.
- JEONG, J., HUSSAIN, F., SCHOPPA, W. & KIM, J. 1997 Coherent structures near the wall in a turbulent channel flow. *J. Fluid Mech.* **332**, 185–214.
- JIMENEZ, J. 2004 Turbulent flows over rough walls. *Annu. Rev. Fluid Mech.* **36** (1), 173–196.
- JIMÉNEZ, J. 2013 Near-wall turbulence. *Phys. Fluids* **25** (10), 9–11.
- JIMÉNEZ, J. 2018 Coherent structures in wall-bounded turbulence. *J. Fluid Mech.* **842**, P1.
- KIM, J. 1989 On the structure of pressure fluctuations in simulated turbulent channel flow. *J. Fluid Mech.* **205**, 421–451.
- KIYA, M. & SASAKI, K. 1985 Structure of large-scale vortices and unsteady reverse flow in the reattaching zone of a turbulent separation bubble. *J. Fluid Mech.* **154**, 463–491.
- KLINE, S., REYNOLDS, W., SCHRAUB, F. & RUNSTADLER, P. 1967 The structure of turbulent boundary layers. *J. Fluid Mech.* **30** (4), 741–773.
- KROGSTAD, P.-Å. & SKÅRE, P.E. 1995 Influence of a strong adverse pressure gradient on the turbulent structure in a boundary layer. *Phys. Fluids* **7** (8), 2014–2024.
- LAMO, D. Á., JUAN, C. & JIMÉNEZ, J. 2009 Estimation of turbulent convection velocities and corrections to Taylor’s approximation. *J. Fluid Mech.* **640**, 5–26.
- LE, H., MOIN, P. & KIM, J. 1997 Direct numerical simulation of turbulent flow over a backward-facing step. *J. Fluid Mech.* **330**, 349–374.

- LEONARDI, S., ORLANDI, P., DJENIDI, L. & ANTONIA, R. 2004 Structure of turbulent channel flow with square bars on one wall. *Intl J. Heat Fluid Flow* **25** (3), 384–392.
- LU, S. & WILLMARTH, W. 1973 Measurements of the structure of the Reynolds stress in a turbulent boundary layer. *J. Fluid Mech.* **60** (03), 481.
- MULLER, A. & GYR, A. 2020 Visualization of the mixing layer behind dunes. In *Mechanics of Sediment Transport*, pp. 41–45. CRC Press.
- MÜLLER, A. & GYR, A. 1986 On the vortex formation in the mixing layer behind dunes. *J. Hydraul. Res.* **24** (5), 359–375.
- NA, Y. & MOIN, P. 1998 Direct numerical simulation of a separated turbulent boundary layer. *J. Fluid Mech.* **374**, 379–405.
- NETO, A., GRAND, D., MÉTAIS, O. & LESIEUR, M. 1993 A numerical investigation of the coherent vortices in turbulence behind a backward-facing step. *J. Fluid Mech.* **256**, 1–25.
- NICKELS, T. & MARUSIC, I. 2001 On the different contributions of coherent structures to the spectra of a turbulent round jet and a turbulent boundary layer. *J. Fluid Mech.* **448**, 367–385.
- ORLANDI, P., LEONARDI, S. & ANTONIA, R. 2006 Turbulent channel flow with either transverse or longitudinal roughness elements on one wall. *J. Fluid Mech.* **561**, 279–305.
- PANTON, R. L. 2001 Overview of the self-sustaining mechanisms of wall turbulence. *Prog. Aerosp. Sci.* **37** (4), 341–383.
- REYNOLDS, W. & HUSSAIN, A. 1972 The mechanics of an organized wave in turbulent shear flow. Part 3. Theoretical models and comparisons with experiments. *J. Fluid Mech.* **54** (2), 263–288.
- ROBINSON, S. K. 1991 Coherent motions in the turbulent boundary layer. *Annu. Rev. Fluid Mech.* **23** (1), 601–639.
- SCHATZMAN, D. & THOMAS, F. 2017 An experimental investigation of an unsteady adverse pressure gradient turbulent boundary layer: embedded shear layer scaling. *J. Fluid Mech.* **815**, 592–640.
- SCHLATTER, P., LI, Q., ÖRLÜ, R., HUSSAIN, F. & HENNINGSON, D. 2014 On the near-wall vortical structures at moderate Reynolds numbers. *Eur. J. Mech. (B/Fluids)* **48**, 75–93.
- SCHOPPA, W. & HUSSAIN, F. 2002 Coherent structure generation in near-wall turbulence. *J. Fluid Mech.* **453**, 57–108.
- SELVATICI, D., QUADRIO, M. & CHIARINI, A. 2023 Curvature effects on the structure of near-wall turbulence. *J. Fluid Mech.* **972**, A39.
- SILLERO, J. A., JIMÉNEZ, J. & MOSER, R. D. 2014 Two-point statistics for turbulent boundary layers and channels at Reynolds numbers up to $\delta^+ \approx 2000$. *Phys. Fluids* **26** (10), 105109.
- SIMPSON, R. 1989 Turbulent boundary-layer separation. *Annu. Rev. Fluid Mech.* **21** (1), 205–232.
- SIMPSON, R. L. 1991 The structure of the near-wall region of two-dimensional turbulent separated flow. *Phil. Trans. R. Soc. Lond. A: Phys. Engng Sci.* **336** (1640), 5–17.
- SONG, S. & EATON, J. 2002 The effects of wall roughness on the separated flow over a smoothly contoured ramp. *Exp. Fluids* **33** (1), 38–46.
- TALAPATRA, S. & KATZ, J. 2012 Coherent structures in the inner part of a rough-wall channel flow resolved using holographic PIV. *J. Fluid Mech.* **711**, 161–170.
- TOWNSEND, A. 1976 *The Structure of Turbulent Shear Flow*, 2nd edn. Cambridge University Press.
- WALLACE, J. M. 2016 Quadrant analysis in turbulence research: history and evolution. *Annu. Rev. Fluid Mech.* **48** (1), 131–158.
- WALLACE, J. M., ECKELMANN, H. & BRODKEY, R. S. 1972 The wall region in turbulent shear flow. *J. Fluid Mech.* **54** (1), 39–48.
- WARK, C. & NAGIB, H. 1991 Experimental investigation of coherent structures in turbulent boundary layers. *J. Fluid Mech.* **230**, 183–208.
- WU, W., MENEVEAU, C. & MITTAL, R. 2020 Spatio-temporal dynamics of turbulent separation bubbles. *J. Fluid Mech.* **883**, A45.
- WU, W. & PIOMELLI, U. 2018 Effects of surface roughness on a separating turbulent boundary layer. *J. Fluid Mech.* **841**, 552–580.
- YAO, J., CHEN, X. & HUSSAIN, F. 2018 Drag control in wall-bounded turbulent flows via spanwise opposed wall-jet forcing. *J. Fluid Mech.* **852**, 678–709.
- ZAMAN, K. & HUSSAIN, A. 1980 Vortex pairing in a circular jet under controlled excitation. Part 1. General jet response. *J. Fluid Mech.* **101** (3), 449–491.
- ZAMAN, K. & HUSSAIN, A. 1981 Turbulence suppression in free shear flows by controlled excitation. *J. Fluid Mech.* **103** (1), 133–159.